ARM: Asteroid Reflection Model

The implementation of an asteroid polarimetry model and its application to interpret asteroid (3200) Phaethon observations

Z.R. Sibbing

Master Thesis Aerospace Engineering

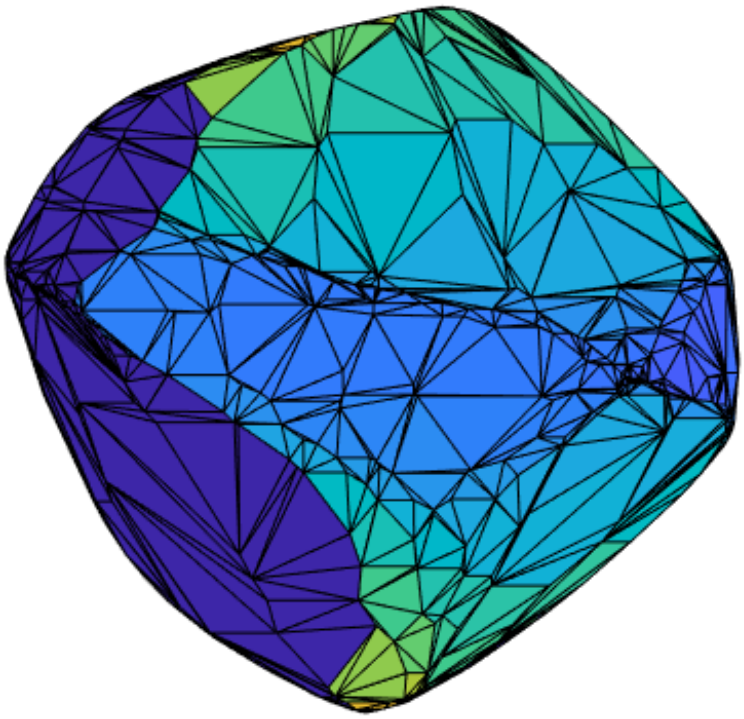

TU Delft

ARM: Asteroid Reflection Model

The implementation of an asteroid polarimetry model and its application to interpret asteroid (3200) Phaethon observations

by

Z.R. Sibbing

Student number:	4108299	
Project duration:	August 14, 2017 – May 24, 2018	
Daily supervisor:	Dr. Daphne M. Stam	
Committee:	Dr.ir. E.J.O. Schrama	Astrodynamics & Space Missions (TU Delft)
	Dr. D.M. Stam	Astrodynamics & Space Missions (TU Delft)
	Dr. A. Menicucci	Space Systems Engineering (TU Delft)
	Dr. S. Bagnulo	Armagh Observatory and Planetarium (UK)

TU Delft

Abstract

Asteroid Reflection Model (ARM) is a newly developed model that simulates reflected radiation and polarization on an asteroid's surface. The working principle behind the model is radiative transfer using Fourier series expansions of reflection matrices. Input models and parameters are: a triangle polyhedron shape model of an asteroid, a surface scattering model, and the desired asteroid location and orientation and the phase angle. Output parameters are the reflected Stokes vector and the degree and direction of polarization, for each individual surface facet and disk-integrated. ARM is fully verified. Generated phase-polarization curves are validated using polarimetric data of four asteroids, including (3200) Phaethon, for which various surface scattering models are deployed. These phase-polarization curves are fit to the Phaethon data, but this did not result in a good match for any of the surface scattering models, since they fail to simulate the opposition effect. However, the effect of the shape, orientation and the rotational motion is clearly visible in the results, as is the relation between wavelength and polarization. Finally, it was concluded that the polarization is favored over the flux when determining an asteroid's surface characteristics and shape, and that both flux and polarization can be used together when determining its size.

Acknowledgments

I would like to thank Daphne for the extensive supervision during the project, the often insightful background information regarding asteroids, the valuable contacts both in the Netherlands and abroad and of course her time. Time that we spent discussing my thesis, looking at figures that I had generated and even debugging my code, which is more often than not a very bad idea. I also thank Stefano Bagnulo and Alberto Cellino for the much appreciated observations of Phaethon, which I could work with although the data was not even published at that time. A great honor. I definitely hope that my thesis might be of interest to them, too, as a means of returning the favor. The work of Karri Muinonen and his team has been an inspiration to me: not only his articles were often helpful, especially in the literature review, but also the SIRIS program was more than welcome. I sure hope that a realistic asteroid surface scattering model is eventually developed thanks to him. Also, I thank Stéphanie Cazaux for having time to visit my mid-term review and ask critical questions.

During my thesis, I spent quite some time at the Aerospace Engineering faculty together with many other students, battling for their master degrees. I guess the battle was slightly less harsh because of the support we always gave each other. Thanks Rutger, Tom and Leon, I hope our motto does really apply to me now! And thanks to Amanthla and Maaike as well, for being the most persistent lunch crew I could have wished for. Finally, there is the support one does not see throughout my thesis or at the faculty, but which are most valuable nonetheless. Thanks mom, dad and Lara and thanks Iris for always being there.

Z.R. Sibbing
Delft, May 6, 2018

Contents

List of Figures

List of Tables

Nomenclature

Abbreviations

APD	Asteroid Polarimetric Database
ARM	Asteroid Reflection Model
AU	Astronomical Unit
DAMIT	Database of Asteroid Models from Inversion Techniques
PDS	Planetary Data System
PRM	Planetary Reflection Model
SPEX	Spectropolarimeter for Planetary EXploration

Roman symbols

$\hat{\mathbf{r}}_{\mathrm{AO}}$	Asteroid-observer vector
$\hat{\mathbf{r}}_{\mathrm{AS}}$	Asteroid-Sun vector
$\mathbf{B}^{+m}$	Diagonal matrix
$\mathbf{c}_{\mathrm{facet}}$	Facet center
$\mathbf{F}^{\mathrm{m}}$	Molecular single scattering matrix
$\mathbf{F}^{\mathrm{p}}$	Particle single scattering matrix
$\mathbf{f}_{\mathrm{facet}}$	Facet coordinate triplet
$\mathbf{I}$	Radiance Stokes vector
$\mathbf{L}$	Rotation matrix
$\mathbf{n}_{\mathrm{facet}}$	Facet normal vector
$\mathbf{p}_{\mathrm{O}}$	Observer's position
$\mathbf{R}$	Reflection matrix
$\mathbf{R}_1^m$	m^{th} Fourier series expansion of $\mathbf{R}_1$
$\mathbf{R}_1$	First column of $\mathbf{R}$
$\mathbf{R}_x$	Rotation matrix around x-axis
$\mathbf{R}_y$	Rotation matrix around y-axis
$\mathbf{R}_z$	Rotation matrix around z-axis
$\mathbf{R}_{\mathrm{total}}$	Total rotation around multiple axes
$\mathbf{s}_{\mathrm{facet}}$	Facet side
$\mathbf{v}_{\mathrm{facet}}$	Vertex coordinates
$\mathbf{v}_{\mathrm{old}}$, $\mathbf{v}_{\mathrm{new}}$	Vector before and after rotation
$\pi\mathbf{F}$	Irradiance Stokes vector
$\pi\mathbf{F}_0$	Incident irradiance Stokes vector
$\pi\mathbf{F}_{\mathrm{observer,\ disk}}$	Disk-integrated irradiance Stokes vector at the observer
$\pi\mathbf{F}_{\mathrm{observer}}$	Irradiance Stokes vector at the observer
$\pi\mathbf{F}_{\mathrm{pixel}}$	Irradiance Stokes vector of one pixel

A	Area
A	Surface albedo
a	Single scattering albedo
a^{m}, b^{m}	Molecular single scattering coefficient
a^{p}, b^{p}	Particle single scattering coefficient
a_{facet}	Facet area
$b^{\mathrm{m}}_{\mathrm{abs}}$	Molecular absorption optical thickness
$b^{\mathrm{p}}_{\mathrm{abs}}$	Particle absorption optical thickness
$b^{\mathrm{m}}_{\mathrm{ext}}$	Molecular extinction optical thickness
$b^{\mathrm{p}}_{\mathrm{ext}}$	Particle extinction optical thickness
$b^{\mathrm{m}}_{\mathrm{sca}}$	Molecular scattering optical thickness
$b^{\mathrm{p}}_{\mathrm{sca}}$	Particle scattering optical thickness
D	Diameter
d	Asteroid-observer distance
F	Irradiance (Stokes element #1)
F	Scattering matrix
f	Facet-to-pixel ratio
F_0	Incident irradiance (Stokes element #1)
F_{ij}	Scattering matrix element (i, j)
I	Radiance (Stokes element #1)
I_{pol}	Polarized intensity
I_{cp}	Circularly polarized intensity
I_{lp}	Linearly polarized intensity
M	Highest Fourier series expansion index
m	Fourier series expansion index
m	Refractive index
n	Number of pixels
n_{abscissa}	Number of Gaussian abscissae
n_{facet}	Number of facets
n_{pixel}	Number of pixels along one dimension
P	Rotational period
$P(r)$	Proper degree of polarization
p_1, p_2, p_3	Coordinate of Cartesian triangle
P_{pixel}	Degree of polarization for one pixel
p_V	Geometric albedo
P_{c}	Circular degree of polarization
$P_{\mathrm{l,max}}$	Maximum linear degree of polarization
$P_{\mathrm{l,min}}$	Minimum linear degree of polarization
P_{l}	Linear degree of polarization
$P_{\mathrm{l}}(X)$	Linear degree of polarization for wavelength filter X
$P_{\mathrm{total,\ mean}}$	Mean total degree of polarization
P_{total}	Total degree of polarization

Q	Linearly polarized radiance (Stokes element #2)
$Q(r)$	Position angle
r	Mean paticle radius
R_{i1}^m	Element i of $\mathbf{R}_1^m$
$r_{\text{facet,max}}$	Maximum facet radius
r_{facet}	Facet radius
t_1, t_2, t_3	Coordinate of barycentric triangle
U	Linearly polarized radiance (Stokes element #3)
V	Circularly polarized radiance (Stokes element #4)
x	Size parameter
y_{pixel}	Horizontal coordinate of a pixel center
z_{pixel}	Vertical coordinate of a pixel center

Greek symbols

α	Phase angle
β	Reference system rotation angle
χ	Direction (or angle) of polarization
χ_{pixel}	Direction (or angle) of polarization for one pixel
χ_{mean}	Mean direction (or angle) of polarization
Δy_{pixel}	Pixel width
Δz_{pixel}	Pixel height
Δ	Variable in the single scattering coefficients
Δ'	Variable in the single scattering coefficients
ϵ_1, ϵ_2	Individual errors
$\epsilon_{\text{orientation}}$	Orientation elevation
ϵ_{total}	Total error
λ	Radiation wavelength
μ	Reflection parameter
μ_0	Incidence parameter
μ_F	Mean F
μ_Q	Mean Q
μ_U	Mean U
μ_V	Mean V
ϕ	Reflection azimuth
$\phi - \phi_0$	Azimuthal difference angle
ϕ_0	Incidence azimuth
$\phi_{\text{orientation}}$	Orientation azimuth
$\pi\mu_{\mathbf{F}}$	Stokes vector mean
$\pi\sigma_{\mathbf{F}}$	Stokes vector standard deviation
ρ	Depolarization factor
Θ	Single scattering angle
θ	Angle of reflection
θ_0	Angle of incidence

Introduction

The field of asteroid polarimetry exists already since the 1930's with discoveries like the negative polarization of the prominent asteroids (1) Ceres and (4) Vesta in 1934 (Dollfus et al., 1989) and the opposition effect of (20) Massalia (Gehrels, 1956). It has been a slowly developing field until the late 1980's when, amongst other developments, narrow opposition effects for (44) Nysa and (64) Angelina were observed (Harris et al., 1989), the coherent backscattering effect established to contribute to asteroid polarimetric effects at small phase angles (Muinonen, 1989; Shkuratov et al., 1994) and generally more polarimetry observations of telescopes became available for interpretation. Mechanisms like these and, for example, multiple-scattering, causing the negative polarization of asteroids, have been subject of research through modeling and observations for the past few decades (Muinonen et al., 2002). Even after the research summary by Muinonen et al. in Asteroids III (Bottke, 2002) was published, yet another fruitful decade of research has passed. Many more observation surveys have been carried out, made possible by the Very Large Telescope (VLT, operative since 2005) and other large telescopes (Belskaya et al., 2015). Observations of near-Earth asteroids (NEA's) (Delbo et al., 2007), some main-belt asteroids (Cellino et al., 2010, 2014), Jupiter Trojans (Belskaya et al., 2014), trans-Neptunian objects (TNO's) (Bagnulo et al., 2008) and more (See Asteroids IV (Michel et al., 2015) for a research summary since 2002), have been done. Furthermore, the Dawn mission has visited (1) Ceres and (4) Vesta, the latter of which has served as a ground truth for regional asteroid surface polarimetry (Cellino et al., 2016) because of the complete polarimetric map of the surface and the observed rotational phase-dependency that were established by earlier observations.

Many new findings have been done with these new observations and techniques for asteroid polarimetry have shed light on asteroid surface properties of interest, improving our general knowledge of asteroid compositions and their ages and origins. A limitation to the current vast amount of observations is that almost all of them are done with Earthly telescopes or space-based telescopes orbiting the Earth. For all asteroids except NEA's and rare asteroids with elliptical orbits, this means that the maximum achievable phase angle is about 30° and rapidly decreases for far away asteroids like TNO's. A harsh limitation indeed, obstructing further mapping of complete phase-polarization curves and obtaining results from those. Because of this, there is still a lot of relevant information untouched. Moreover, hardly any asteroid has been observed with a dedicated spacecraft polarimeter, providing the possibility of increased phase angles and, obviously, a higher spatial resolution if the spacecraft gets close enough (Muinonen et al., 2002). Fortunately, the Spectropolarimeter for Planetary EXploration (SPEX) is a good candidate for this purpose (Snik et al., 2010; Voors et al., 2011; van Harten, 2014).

Modeling asteroid polarimetry with SPEX was de first and most important driver for this thesis, therefore it is thoroughly discussed in the literature review associated with this thesis (Sibbing, 2017). The research objective of this literature review was *"to contribute to the SPEX polarimetry instrument by defining requirements and design specifications for its specific application to asteroid observations"*. The application of SPEX to asteroid observations is still quite conceptual, though, and it was decided during this research that modeling asteroid polarimetry, in combination with the analysis of available polarimetric data, is a more suitable topic at this time, and very much related to the previous topic. Hence the Asteroid Reflection Model (ARM) was developed, theoretically based on the Planetary Reflection Model (PRM) for (exo)planets (Rossi et al., 2018). ARM aims to model the reflected radiation and polarization of an asteroid of any shape and size, using an arbitrary surface scattering model. Doing so, it can simulate and fit available polarimetric data of an asteroid and support conclusions regarding these data. No model such as ARM, that take into account the asteroid shape (as opposed to a spherical shape) *and* calculate the polarization, exists at this time, which makes this work novel.

The research objective of this thesis is *to determine the influence of the surface, shape and orientation of an asteroid on its reflected radiation and polarization by modeling it and fitting it to available polarimetric observations*. The first part of this research objective is covered by ARM. The second part is realized by ana-

lyzing polarimetric data of multiple asteroids, including Phaethon, of which data was acquired as recent as in December 2017 by Cellino et al. (2018). Analyzing these data and fitting them is a very interesting early application of ARM which proves its usability in the field of asteroid polarimetry.

The structure of this thesis, supporting the research objective, is as follows. Chapter 1 describes the essential theory used in ARM and its working principles. It is subdivided into Section 1.1, where the theory of polarization (Hansen and Travis, 1974) and radiative transfer (De Haan et al., 1987; Rossi et al., 2018) is discussed, Section 1.2, where the asteroid's shape model is discussed, and Section 1.3, where a modeled instrument detector and additional ARM functionalities are introduced. Chapter 2 discusses the verification of ARM in five verification tests, subdivided into tests regarding the model fundamentals (Section 2.1) and the output in terms of polarization (Section 2.2). Chapter 3 finally assesses the results of ARM as generated here. First, in Section 3.1, the surface scattering models used in the simulations, are discussed. Next, in Section 3.2 and Section 3.3, the spatially resolved results and the phase-polarization results, following from ARM, are discussed respectively. Last, in Section 3.4, the special case of asteroid Phaethon is discussed, again including both spatially resolved and phase-polarization results and this time also phase-flux results. Finally, conclusions are drawn and recommendations are given adequately.

1

Modeling asteroid polarimetry

This chapter discusses ARM in three steps. The theoretical basis for polarization and the radiative transfer method is discussed in Section 1.1, covering material from Rossi et al. (2018), which has served as an important impulse for this thesis. The model that allows any asteroid of which a polyhedron model is available to serve as input for ARM, is discussed in Section 1.2, including the principles used to implement the effect of self-shading on an asteroid model. Section 1.3 assesses the transition from asteroid model to detector (effectively modeling SPEX) and additional features that make ARM generally more useful for its applications.

1.1. Radiative transfer with reflection matrices

1.1.1. Reference systems and translations

In order to use the radiative transfer method correctly and efficiently, several reference systems will be defined here and referred to later on. It will be shown that this is necessary to calculate fundamental angles and the translation to a modeled detector for reflected radiation.

- **Asteroid body reference system**. This reference system follows directly from the shape model. Principle x-, y- and z-axes are given through the coordinates of the vertices of the polyhedron.
- **Heliocentric ecliptic reference frame**. With the Sun at the origin and the ecliptic as the xy-plane, this reference system is convenient for positions with regard to the Solar System. The z-axis is directed to the celestial north pole. See Wakker (2015, p.250-251).
- **Local meridian plane system**. The origin coincides with the center of mass of the asteroid and the x-axis coincides with the asteroid-observer vector, $\hat{\mathbf{r}}_{\mathrm{AO}}$. The y-axis lies 90° away in the direction of the facet normal and such that the facet normal, $\hat{\mathbf{n}}_{\mathrm{facet}}$, lies in the xy-plane. The z-axis completes the right-handed system, thus pointing in the direction of $\hat{\mathbf{r}}_{\mathrm{AO}} \wedge \hat{\mathbf{n}}_{\mathrm{facet}}$.
- **Planetary scattering plane system**. The origin coincides with the center of mass of the asteroid and the x-axis coincides with $\hat{\mathbf{r}}_{\mathrm{AO}}$. The y-axis lies 90° away such that the asteroid-Sun vector, $\hat{\mathbf{r}}_{\mathrm{AS}}$, lies in the xy-plane. The z-axis completes the right-handed system such that it lies in the northern hemisphere of the heliocentric ecliptic reference system ('above' the Earth's orbital plane).
- **Planetary scattering plane system (Sun-faced)**. The origin coincides with the center of mass of the asteroid and the x-axis coincides with $\hat{\mathbf{r}}_{\mathrm{AS}}$. The y-axis lies 90° away such that the asteroid-observer vector, $\hat{\mathbf{r}}_{\mathrm{AO}}$, lies in the xy-plane. The z-axis completes the right-handed system such that it lies in the northern hemisphere of the heliocentric ecliptic reference system. This reference system is effectively the planetary scattering plane system rotated by $\pm\alpha$ around the z-axis.

1.1.2. Principles of polarization

The basics of polarization of radiation have all been discussed in the literature study associated with this thesis (Sibbing, 2017) and in Rossi et al. (2018), which has served as an example for this work in many ways. The same conventions regarding polarization parameters and the Stokes vector are used here. In Hansen and Travis (1974), the definitions of the different radiation intensities are given as follows, consisting of terms for linear part, I_{lp}, and the circular part, I_{cp}. See Equation 1.1.

$$I_{\text{pol}} = \left(I_{lp}^2 + I_{cp}^2\right)^{1/2} \tag{1.1}$$

The degrees of linear and circular polarization come from the Stokes vector, **I**, consisting of Stokes parameters I, Q, U, and V. Parameter I is the total radiance, Q and U represent the linearly polarized radiance and V the circularly polarized radiance, all in units W m^{-2} sr^{-1}. The irradiance, $\pi\mathbf{F}$, with units W m^{-2}, is an alternative representation of the Stokes vector containing terms analogous to those in **I** and is given in Equation 1.2. This convention of the Stokes vector is used from here onward.

$$\pi\mathbf{F} = \pi \begin{bmatrix} F \\ Q \\ U \\ V \end{bmatrix} \tag{1.2}$$

Expressing the linear and circular degrees of polarization in elements from the Stokes vector of Equation 1.2 leads to Equation 1.3 to Equation 1.5.

$$P_{\text{total}} = \frac{\sqrt{Q^2 + U^2 + V^2}}{F} \tag{1.3}$$

$$P_{\text{l}} = \frac{\sqrt{Q^2 + U^2}}{F} \tag{1.4}$$

$$P_{\text{c}} = \frac{V}{F} \tag{1.5}$$

where P_{l} and P_{c} are the degrees of linear and circular polarization, respectively.

Parameters Q and U require a reference system with respect to which they are defined. In this reference system, Q is then defined as the horizontally polarized irradiance minus the vertically polarized irradiance, or, $Q = F_{0^\circ} - F_{90^\circ}$. Similarly, U is defined as $U = F_{45^\circ} - F_{135^\circ}$, rotated 45° compared to Q. Initially, Q and U are defined locally, for each facet, in the local meridian plane system. Since each facet has its own reference system, all have to be translated to the planetary scattering plane system.

The angle between these two reference systems is β, which can be calculated using projections of a surface facet's normal vector, $\hat{\mathbf{n}}_{\text{facet}}$, and $\mathbf{r}_{\text{AS}}$, both in the observer direction. The angle between these two vectors in the described projection plane (the yz-plane of the planetary scattering plane system) is β, which is defined as rotating clockwise when looking from the observer to the asteroid. The limits for β are $0^\circ \leq \beta < 180^\circ$, which effectively means that 180° should be subtracted from β if the surface facet normal has a negative z-value in the planetary scattering plane system (which is the case for the entire southern hemisphere of a spherical body).

Rotating the Stokes vector along an angle β is done using the rotation matrix **L** (Hovenier and Van der Mee, 1983), given in Equation 1.6.

$$\mathbf{L}(\beta) = \begin{bmatrix} 1 & 0 & 0 & 0 \\ 0 & \cos 2\beta & \sin 2\beta & 0 \\ 0 & -\sin 2\beta & \cos 2\beta & 0 \\ 0 & 0 & 0 & 1 \end{bmatrix} \tag{1.6}$$

The degree of polarization P_{total} comes with a direction (or angle) of polarization, χ. This angle depends on the chosen reference system, which would be the planetary scattering plane system when considering the polarization integrated over a body. By definition, χ is given by:

$$\tan 2\chi = \frac{U}{Q} \tag{1.7}$$

where χ is from $0° \leq \chi < 180°$ such that $\cos 2\chi$ has the same sign as Q (Hansen and Travis, 1974). Because of the $\tan 2\chi$ in Equation 1.7, there are always two solutions to this equation within the limits of χ: 90° can be added to or subtracted from χ in order to fulfill the Q-sign convention. In the case of $U = 0$, the two options are perpendicular polarization ($Q < 0$ with $\chi = 90°$) and parallel polarization ($Q > 0$ with $\chi = 0°$). Because the sum of squares in Equation 1.4 would shroud the sign of Q, an alternative expression for the linear polarization is used if $U = 0$. See Equation 1.8

$$P_l = \frac{-Q}{F} \tag{1.8}$$

1.1.3. The reflected Stokes vector

In order to calculate the reflected Stokes vector, formulations for the incident Stokes vector, including reference frames, have been discussed so far. According to Hansen and Travis (1974), the general equation for the reflected Stokes vector is:

$$\mathbf{I}(\mu, \mu_0, \phi - \phi_0) = \mu_0 \mathbf{R}(\mu, \mu_0, \phi - \phi_0)\mathbf{F}_0 \tag{1.9}$$

with $\pi\mathbf{F}_0$ the Stokes flux vector of the incident light and $\mathbf{R}$ the 4×4 reflection matrix. Incidence and reflection parameters, μ_0 and μ, respectively, are derived from the angles of incidence and reflection for each facet, θ_0 and θ, and are defined as $\mu_0 = \cos\theta_0$ and $\mu = \cos\theta$.

A convenient way to calculate μ_0 and μ is through the dot product of the facet normal with $\hat{\mathbf{r}}_{\mathrm{AS}}$ and $\hat{\mathbf{r}}_{\mathrm{AO}}$, respectively, after which θ_0 and θ follow. See Equation 1.10 to Equation 1.13.

$$\mu_0(n) = \hat{\mathbf{n}}_{\mathrm{facet}}(n) \cdot \hat{\mathbf{r}}_{\mathrm{AS}} \tag{1.10}$$

$$\mu(n) = \hat{\mathbf{n}}_{\mathrm{facet}}(n) \cdot \hat{\mathbf{r}}_{\mathrm{AO}} \tag{1.11}$$

$$\theta_0(n) = \arccos\mu_0 \tag{1.12}$$

$$\theta(n) = \arccos\mu \tag{1.13}$$

The azimuthal difference angle in Equation 1.9, $\phi - \phi_0$, is defined as 180° minus the angle between the local vertical plane of incidence (hence ϕ_0) and the local vertical plane of reflection (hence ϕ), clockwise when looking from the observer to the asteroid. In this way, the azimuthal difference angle is limited to $-180° \leq \phi - \phi_0 \leq 180°$, with negative values occurring when the angle between the local planes exceeds 180°, keeping to the clockwise convention. In the simple case of specular reflection, reflection in the half of the plane containing the Sun, results in $\phi - \phi_0 = \pm 180°$. Reflection in the other half results in $\phi - \phi_0 = 0°$.

The incident sunlight is assumed to be unpolarized, therefore the Stokes vector $\mathbf{F}_0$ equals $F_0[1,0,0,0]^{\mathrm{T}}$, F_0 being the incident flux parallel to the direction of incidence, divided by π (Hansen and Travis, 1974). Because of the three zero terms in $\mathbf{F}_0$, the columns of $\mathbf{R}$ corresponding to those zero terms can be ignored. The only column of importance is the first one, denoted by $\mathbf{R}_1$. The elements of $\mathbf{R}_1$ are provided by an external program (Fourier Series Program, see Rossi et al. (2018)) that makes use of Fourier expansions for $\mathbf{R}_1$, as discussed by De Haan et al. (1987). The simplified version of Equation 1.9, using parameters $\mathbf{R}_1$ and F_0, is given in Equation 1.14.

$$\mathbf{I}(\mu, \mu_0, \phi - \phi_0) = \mu_0 \mathbf{R}_1(\mu, \mu_0, \phi - \phi_0)F_0 \tag{1.14}$$

To determine which fraction of this reflected flux arrives at the observer, the distance between the asteroid and the observer, d, is needed. See Equation 1.15. For each surface facet, the incident and reflected flux are calculated separately. Elements of the Stokes vector are only added later to obtain the disk-integrated values.

$$\pi\mathbf{F}_{\mathrm{observer}} = \frac{1}{d^2}\mu\mathbf{I}(\mu, \mu_0, \phi - \phi_0)dA = \frac{1}{d^2}\mu\mu_0\mathbf{R}_1(\mu, \mu_0, \phi - \phi_0)F_0 dA \tag{1.15}$$

where A represents the area. The factor with which $\mathbf{I}(\mu, \mu_0, \phi - \phi_0)$ was multiplied in order to scale it to the observer thus amounts to $\frac{1}{d^2}\mu dA$. The disk-integrated Stokes vector arriving at the observer is then obtained by integrating over all the facets and is given in Equation 1.16 (from Stam et al. (2006)).

$$\pi\mathbf{F}_{\mathrm{observer,\ disk}} = \pi\int_A \mathbf{F}_{\mathrm{observer}} = \frac{1}{d^2}\int_A \mu\mu_0\mathbf{R}_1(\mu, \mu_0, \phi - \phi_0)F_0 dA \tag{1.16}$$

Still, $\pi \mathbf{F}_{\text{observer, disk}}$ is in units W m^{-2}.

Both planetary (or asteroid) surfaces and planetary atmospheres are accounted for in the Fourier Series Program and they are dealt with separately. The reflection principles for an asteroid surface are relatively simple as compared to a hypothetical atmosphere. Consider a smooth and clean surface without regolith and the reflection can be approximated by Lambertian reflection, isotropically and unpolarized, if the incident light was indeed unpolarized as well. Another option is Fresnel reflection, which is non-isotropic and results in polarized radiation. This option, however, has not been included in the Fourier Series Program as of yet. Apart from the reflection model, the surface albedo can be set and is defined as the ratio of surface reflected radiation to surface incident radiation.

The physics of atmospheric reflection are relevant to the application of the Fourier Series Program to asteroids because a potential regolith sheet can be modeled as an extremely dense and thin atmosphere of some kind of composition. The program distinguishes gas molecules and (solid) aerosol particles, which are the regolith particles in this case. The single scattering matrix for Rayleigh scattering of gas molecules is described by (Hansen and Travis, 1974), see Equation 1.17.

$$\mathbf{F}^{\text{m}}(\Theta) = \begin{bmatrix} a_1^{\text{m}}(\Theta) & b_1^{\text{m}}(\Theta) & 0 & 0 \\ b_1^{\text{m}}(\Theta) & a_2^{\text{m}}(\Theta) & 0 & 0 \\ 0 & 0 & a_3^{\text{m}}(\Theta) & 0 \\ 0 & 0 & 0 & a_4^{\text{m}}(\Theta) \end{bmatrix} \tag{1.17}$$

with coefficients for $a^{\text{m}}(\Theta)$ and $b^{\text{m}}(\Theta)$ as follows:

$$\begin{aligned} a_1^{\text{m}}(\Theta) &= 1 - \frac{1}{4}\Delta(1 - 3\cos^2\Theta) \\ a_2^{\text{m}}(\Theta) &= \frac{3}{4}\Delta(1 + \cos^2\Theta) \\ a_3^{\text{m}}(\Theta) &= \frac{3}{2}\Delta\cos\Theta \\ a_4^{\text{m}}(\Theta) &= \frac{3}{2}\Delta\Delta'\cos\Theta \\ b_1^{\text{m}}(\Theta) &= -\frac{3}{4}\Delta\sin^2\Theta \end{aligned}$$

with

$$\Delta = \frac{1-\rho}{1+\rho/2} \quad \text{and} \quad \Delta' = \frac{1-2\rho}{1+\rho/2}$$

where ρ represents the depolarization factor, which depends on the wavelength (Bates, 1984). The coefficients as stated above themselves are not provided by the Fourier Series Program, instead, the Fourier expansion coefficients of $\mathbf{F}^{\text{m}}(\Theta)$ are given. The atmospheric model allows for multiple atmospheric layers, each with a gaseous extinction optical thickness, $b_{\text{ext}}^{\text{m}}$, which is a sum of the scattering optical thickness, $b_{\text{sca}}^{\text{m}}$, and the absorption optical thickness, $b_{\text{abs}}^{\text{m}}$, all defined in the vertical direction.

Similar to the molecule single scattering matrix is the particle single scattering matrix, $\mathbf{F}^{\text{p}}(\Theta)$, see Equation 1.18.

$$\mathbf{F}^{\text{p}}(\Theta) = \begin{bmatrix} a_1^{\text{p}}(\Theta) & b_1^{\text{p}}(\Theta) & 0 & 0 \\ b_1^{\text{p}}(\Theta) & a_2^{\text{p}}(\Theta) & 0 & 0 \\ 0 & 0 & a_3^{\text{p}}(\Theta) & b_2^{\text{p}}(\Theta) \\ 0 & 0 & -b_2^{\text{p}}(\Theta) & a_4^{\text{p}}(\Theta) \end{bmatrix} \tag{1.18}$$

Again, the model provides Fourier elements rather than the coefficients in Equation 1.18. Also similar to the case of molecule single scattering, extinction, scattering and absorption optical thicknesses are given by $b_{\text{ext}}^{\text{p}}$, $b_{\text{sca}}^{\text{p}}$ and $b_{\text{abs}}^{\text{p}}$, respectively, where the extinction optical thickness is the sum of the other two. The single scattering albedo of the particles, analogous to the asteroid surface albedo, is given by the ratio $b_{\text{sca}}^{\text{p}}/(b_{\text{sca}}^{\text{p}} + b_{\text{abs}}^{\text{p}})$. Potential wavelength dependence of one or more of the particle layers is incorporated in with wavelength dependence of the particles the layer is composed of. The algorithm in the Fourier Series Program accepts either particles that are spherical, that have a plane of symmetry in an arbitrary orientation or particles that are asymmetrical and arbitrarily oriented while each particle has a mirror particle. In the latter case, one half of the particles mirrors the other half.

Finally, combining Equation 1.17 and Equation 1.18 to define a single matrix for the atmosphere or regolith layer, is done through Equation 1.19.

$$\mathbf{F}(\Theta) = \frac{b^{\mathrm{m}}_{\mathrm{sca}}\mathbf{F}^{\mathrm{m}}(\Theta) + b^{\mathrm{p}}_{\mathrm{sca}}\mathbf{F}^{\mathrm{p}}(\Theta)}{b^{\mathrm{m}}_{\mathrm{sca}} + b^{\mathrm{p}}_{\mathrm{sca}}} \tag{1.19}$$

The single scattering albedo is combined through Equation 1.20.

$$a = \frac{b^{\mathrm{m}}_{\mathrm{sca}} + b^{\mathrm{p}}_{\mathrm{sca}}}{b^{\mathrm{m}}_{\mathrm{sca}} + b^{\mathrm{p}}_{\mathrm{sca}} + b^{\mathrm{m}}_{\mathrm{abs}} + b^{\mathrm{p}}_{\mathrm{abs}}} \tag{1.20}$$

1.1.4. Fourier series expansion of $\mathbf{R}_1$

In Section 1.1.3, it was discussed that only the first column of reflection matrix $\mathbf{R}$ is needed: $\mathbf{R}_1$. In De Haan et al. (1987), an equation to expand such a reflection matrix into a Fourier series is shown. This equation is rewritten as follows, as to keep only the first column of $\mathbf{R}$.

$$\mathbf{R}_1(\mu,\mu_0,\phi-\phi_0) = \mathbf{B}^{+0}(\phi-\phi_0)\mathbf{R}^0_1(\mu,\mu_0) + 2\sum_{m=1}^{M}\mathbf{B}^{+m}(\phi-\phi_0)\mathbf{R}^m_1(\mu,\mu_0) \tag{1.21}$$

with $\mathbf{R}^m_1(\mu,\mu_0)$ the first column of the m^{th} Fourier series matrix, with $(0 \le m \le M)$, and $\mathbf{B}^{+m}$ a diagonal matrix containing terms for $m\phi$ as follows:

$$\mathbf{B}^{+m}(\phi) = \begin{bmatrix} \cos m\phi & 0 & 0 & 0 \\ 0 & \cos m\phi & 0 & 0 \\ 0 & 0 & \sin m\phi & 0 \\ 0 & 0 & 0 & \sin m\phi \end{bmatrix} \tag{1.22}$$

An advantage of using the terms $\mathbf{R}^m_1(\mu,\mu_0)$ in the expansion of Equation 1.21 is that all are independent of the azimuthal difference $\phi-\phi_0$, which is relocated entirely to the equation of $\mathbf{B}^{+m}(\phi)$, in Equation 1.22.

Next, Equation 1.9, Equation 1.21 and Equation 1.22 can be combined into relations for the four Stokes vector elements as follows.

$$I(\mu,\mu_0,\phi-\phi_0)/\mu_0 F_0 = R^0_{11}(\mu,\mu_0) + 2\sum_{m=1}^{M}\cos m(\phi-\phi_0)R^m_{11}(\mu,\mu_0) \tag{1.23}$$

$$Q(\mu,\mu_0,\phi-\phi_0)/\mu_0 F_0 = R^0_{21}(\mu,\mu_0) + 2\sum_{m=1}^{M}\cos m(\phi-\phi_0)R^m_{21}(\mu,\mu_0) \tag{1.24}$$

$$U(\mu,\mu_0,\phi-\phi_0)/\mu_0 F_0 = 2\sum_{m=1}^{M}\sin m(\phi-\phi_0)R^m_{31}(\mu,\mu_0) \tag{1.25}$$

$$V(\mu,\mu_0,\phi-\phi_0)/\mu_0 F_0 = 2\sum_{m=1}^{M}\sin m(\phi-\phi_0)R^m_{41}(\mu,\mu_0) \tag{1.26}$$

where the subscripts 11 to 41 of R^0 and R^m denote the 1^{st} to 4^{th} element of the vectors R^0_1 and R^m_1, respectively. These elements are finally provided by the Fourier Series Program, for $(0 \le m \le M)$. The calculations of these elements follow from the adding-doubling algorithm (De Haan et al., 1987).

The adding-doubling algorithm is an algorithm based on dividing an atmosphere into layers for which separate upward and downward scattering matrices are calculated. First, of each layer, the reflection and transmission properties have to be known. Two adjacent layers can be combined into one layer as follows. The top layer is assumed to be illuminated from above. Part of the light is already absorbed by the top layer, part is transmitted to the bottom layer once it encounters the boundary, and part is reflected by the bottom layer back into the top layer. The events of transmission and reflection repeat itself in the top layer and bottom layer several times, after which the total transmission and reflection of the combined layer can be calculated. Following this approach, the newly combined layer can be combined with an adjacent layer, after which yet another layer can be added and so on. Hence the adding method. A requirement for the adding method is that

both atmospheric layers are homogeneous: scattering properties may only vary with optical thickness. However, the layers don't need to be identical, which is what the doubling method is for. The doubling method is meant to double a homogeneous layer with known scattering properties. Again, the adding method is used to add an identical layer which results in the same atmospheric layer with double the optical thickness. This process can be repeated as often as needed. Doubling thus is a simplification of adding. For the complete adding method, see De Haan et al. (1987).

The Fourier Series Program database contains Fourier coefficients for various predefined values of μ and μ_0, values that correspond to Gaussian abscissae used in the adding-doubling algorithm to integrate over all scattering directions. For a given number of abscissae, n_{abscissa}, the number of (μ, μ_0) combinations is n^2_{abscissa}, which makes it not very computationally attractive to make this number to high. In practice, only the Fourier coefficients of an abscissa that corresponds exactly to a (μ, μ_0) combination can be used directly. For all other combinations, interpolation of abscissae, and thus of Fourier coefficients, has to be used. The interpolation as used here is spline interpolation (Press et al., 1996, p. 1044-1045). The (μ, μ_0) combinations have a default range of $0 < (\mu, \mu_0) < 1$ so an extra abscissa is added to include $\mu, \mu_0 = 1$, to facilitate in this very common value. All other abscissae are distributed such that the spacing between abscissae is according to a Gaussian distribution: near $\mu, \mu_0 = 0$ and $\mu, \mu_0 = 1$, the spacing is small, and it increases from both sides symmetrically towards a maximum spacing around $\mu, \mu_0 = 0.5$.

The accuracy of the radiative transfer computations depends on the number of Gaussian abscissae and the scattering properties of the surface scattering models that are used. Strongly varying scattering properties will need to be compensated by many abscissae, whereas smooth scattering properties will result in the same accuracy using fewer abscissae. Adding abscissae locally could be used as a method to improve the accuracy where the scattering properties vary most, if this is known upfront or through practice.

1.2. Asteroid polyhedron model

The topic of this section is to introduce the way in which an asteroid's shape is incorporated in ARM and to introduce the method of calculating self-shading of an asteroid model.

1.2.1. Polyhedron geometry

An important requirement for an asteroid model with which surface reflection can be modeled, is that the surface faces are 2-dimensional. Polyhedrons are a family of 3-dimensional geometrical objects consisting of many 2-dimensional polygons in such a way that there are no empty spaces in its boundary surface. Part of this family are polyhedrons consisting only of triangles of different sizes. Since many existing asteroid models use this convention, it is very convenient to choose this type of model as a basis for the cause of modeling polarimetry. The DAMIT database (Ďurech et al., 2010; Ďurech, 2018) contains many of these asteroid polyhedron models, computed using inversion techniques. The Planetary Data System contains radar shape models and optical shape models (Neese, 2004; NASA, 2018) both of which can be used in addition to the DAMIT database models.

The asteroid models come with an array of x-, y- and z-coordinates for the vertices of the polyhedron and an array of groups of 3 integers giving the numbers of the vertices that form a facet of the polyhedron. Obviously, every vertex is used at least in one facet or it would be redundant. Several interesting parameters regarding this asteroid model can be calculated relatively easily: the center of each facet, $\mathbf{c}_{\text{facet}}$, the normal vector of each facet, $\hat{\mathbf{n}}_{\text{facet}}$, the area of each facet, a_{facet}, the facet radius (the distance from the barycenter of the asteroid to the facet center), r_{facet}, and the maximum facet radius, as a measure for a hypothetical sphere in which the entire asteroid would fit, $r_{\text{facet,max}}$. These parameters will prove themselves very useful throughout the rest of the Asteroid Reflection Model (ARM). Table 1.1 gives an overview of these parameters and their equations. The only non-trivial equation is the equation for the facet area, which is a variant of Heron's formula (Weisstein, 2018b).

The asteroid shape model that is obtained so far can be put in a location in space in different ways. Looking ahead to the directions of incident and reflected sunlight, discussed shortly, one would like to be able to set

Table 1.1: An overview of the geometrical parameters derived from parameters from the asteroid polyhedron model, their symbols, dimensions and the equation with which they are calculated. The equation for the facet area comes from Heron's formula (Weisstein, 2018b).

Parameter	**Symbol**	**Dimensions**	**Equation**
Vertices	$\mathbf{v}_{\text{facet}}$	$3 \times n_{\text{facet}}$	-
Facet coordinates	$\mathbf{f}_{\text{facet}}$	$3 \times 3 \times n_{\text{facet}}$	-
Facet center	$\mathbf{c}_{\text{facet}}$	$3 \times n_{\text{facet}}$	$\mathbf{c}_{\text{facet}}(n) = \frac{1}{3}\sum_{i=1}^{3} \mathbf{f}_{\text{facet}}(:, i, n)$
Facet normal	$\hat{\mathbf{n}}_{\text{facet}}$	$3 \times n_{\text{facet}}$	$\hat{\mathbf{n}}_{\text{facet}}(n) = \{(\mathbf{f}_{\text{facet}}(:,2,n) - \mathbf{f}_{\text{facet}}(:,1,n)) \wedge (\mathbf{f}_{\text{facet}}(:,3,n) - \mathbf{f}_{\text{facet}}(:,1,n))\} / \lvert\lvert(\mathbf{f}_{\text{facet}}(:,2,n) - \mathbf{f}_{\text{facet}}(:,1,n)) \wedge (\mathbf{f}_{\text{facet}}(:,3,n) - \mathbf{f}_{\text{facet}}(:,1,n))\rvert\rvert$
Facet sides	$\mathbf{s}_{\text{facet}}$	$3 \times n_{\text{facet}}$	$\mathbf{s}_{\text{facet}}(i_1, n) = \sqrt{\sum_{j=1}^{3} (\mathbf{f}_{\text{facet}}(j, i_1, n) - \mathbf{f}_{\text{facet}}(j, i_2, n))^2}$ with $\{i_1, i_2\} = \{1,2\}, \{2,3\}$ and $\{3,1\}$
Facet area	a_{facet}	$1 \times n_{\text{facet}}$	$a_{\text{facet}}(n) = \frac{1}{4}\{(\mathbf{s}_{\text{facet}}(1,n) + \mathbf{s}_{\text{facet}}(2,n) - \mathbf{s}_{\text{facet}}(3,n)) (\mathbf{s}_{\text{facet}}(1,n) - \mathbf{s}_{\text{facet}}(2,n) + \mathbf{s}_{\text{facet}}(3,n)) (-\mathbf{s}_{\text{facet}}(1,n) + \mathbf{s}_{\text{facet}}(2,n) + \mathbf{s}_{\text{facet}}(3,n)) (\mathbf{s}_{\text{facet}}(1,n) + \mathbf{s}_{\text{facet}}(2,n) + \mathbf{s}_{\text{facet}}(3,n))\}^{1/2}$
Facet radius	r_{facet}	$1 \times n_{\text{facet}}$	$r_{\text{facet}}(n) = \sqrt{\sum_{i=1}^{3} (\mathbf{c}_{\text{facet}}(i,n))^2}$
Maximum r_{facet}	$r_{\text{facet,max}}$	1	$r_{\text{facet,max}} = \max(r_{\text{facet}}(n))$ with $n = 1...n_{\text{facet}}$

the phase angle, α, to a certain value. Realistically, though, it would make sense to just set the location of the asteroid and the location of the observer to certain values. As a result, two different input methods are distinguished. The Sun's location is at the barycenter of the Solar System and the asteroid is at some realistic fixed location at about 1 AU distance of the Sun. Next, in the first case, the observer is at some distance, typically half the distance between the Sun and the asteroid, with an adjustable phase angle. In the second case, the observer's location is completely free and the phase angle follows from it. The orientation and rotation of the asteroid in its body reference system are discussed in Section 1.3.

1.2.2. Self-shading

Many asteroids have shapes so irregular that shading from one facet onto another is likely to occur. This phenomenon of self-shading finds itself somewhere between the geometry and the radiative transfer parts of ARM. The shading that is taken into account is exclusively first order shading: only a facet which directly blocks incoming sunlight casts a shadow on another facet. No shading as a result of higher order scattering is incorporated in ARM. Since the calculations in the model are very much geometry-based, it is discussed here.

The process to determine the correct facets that are both illuminated and observable by the observer, taking into account self-shading, has been implemented in four phases, two for incident and two for reflected radiation. Each phase removes a certain number of facets from the considered pool of possibly illuminated facets under certain conditions, keeping only the truly illuminated facets in the end. The first phase removes about half of the facets by imposing the condition $\mu_0 > 0$. Those facets that are not facing the Sun are removed.

The second phase calculates self-shading in the Sun-asteroid direction. For each facet i that is left after phase one, a semi-infinite volume stretching behind the facet in the Sun-asteroid direction with a base equal to a projection of this facet in the Sun-asteroid direction, is searched for values of $\mathbf{c}_{\text{facet}}(j)$. The search for a point in the interior of a 2-dimensional triangle is done using barycentric coordinates (Weisstein, 2018a). The equations for the coordinates of barycentric triangle $\triangle t_1 t_2 t_3$, are given as a function of the coordinates of Cartesian triangle $\triangle p_1 p_2 p_3$, in Equation 1.27 to Equation 1.29. The point to be searched for is indicated by p.

$$t_1 = \frac{(p_{2,y} - p_{3,y})(p_z - p_{3,z}) + (p_{3,z} - p_{2,z})(p_y - p_{3,y})}{(p_{2,y} - p_{3,y})(p_{1,z} - p_{3,z}) + (p_{3,z} - p_{2,z})(p_{1,y} - p_{3,y})} \tag{1.27}$$

$$t_2 = \frac{(p_{3,y} - p_{1,y})(p_z - p_{3,z}) + (p_{1,z} - p_{3,z})(p_y - p_{3,y})}{(p_{2,y} - p_{3,y})(p_{1,z} - p_{3,z}) + (p_{3,z} - p_{2,z})(p_{1,y} - p_{3,y})} \tag{1.28}$$

$$t_3 = 1 - t_1 - t_3 \tag{1.29}$$

The constraints for point p to lie within the boundaries of triangle $\triangle t_1 t_2 t_3$ are: $t_1 > 0$, $t_2 > 0$ and $t_3 > 0$. The constraints for $\mathbf{c}_{\text{facet}}(j)$ to lie within the shading volume of facet i thus are the previously mentioned three and the constraint that $\mathbf{c}_{\text{facet}}(j)$ lies behind $\mathbf{c}_{\text{facet}}(i)$ in the Sun-asteroid direction. All the facets found in this way are removed from the pool of considered facets after this phase is completed.

The third phase continues with the facets left after phase two and removes all the facets with $\mu < 0$, facets that are illuminated by the Sun but that are not facing the observer. The fourth phase completes the algorithm by searching a similar self-shading volume as in phase two, this time in the observer-asteroid direction. Typically, phase one removes 50% of the facets, phase three removes a percentage proportional to $\frac{1}{2}\sin\alpha$ and phase two and four remove another 0-5% each, depending on the irregularity of the asteroid shape and surface.

Irregardless of the effectiveness, this search algorithm is quite inefficient because the number of operations that is executed in phase two equals the number of facets left after phase one, squared, and in phase four the number of facets left after phase three, squared. For large asteroid shape models, this algorithm quickly becomes the bottle neck of the entire simulation. Another inevitability is that a facet near the edge of the Sun-asteroid projection of the asteroid could be blocked for up to almost 50% and still have its center outside the searched volume. It is considered to be fully illuminated as a result. Similarly, a facet which is blocked for just over 50% is considered to be fully shaded, due to the location of $\mathbf{c}_{\text{facet}}$.

A possible solution to this problem is to consider facets in greater detail by dividing them into sub-facets. One could indeed create a more detailed model by splitting some or all facets into multiple sub-facets. The problem with this method, however, is that all sub-facets then have the same normal direction as their parent facet, which means that this newly created polyhedron does not offer the accuracy one would want from a polyhedron model with actually more facets (including realistic normal directions). Although solutions could be found to solve this, these would amount to estimating a more detailed polyhedron model instead of actually having it at one's disposal. For example, the normal direction of a sub-facet could be set to an average value of the normal direction of the parent facet and the nearest neighboring facet. Further investigating the accuracy and realisticness of polyhedron models is beyond the scope of this research.

1.3. Transition to instrument and additional features

In Section 1.1, relations have been discussed to determine the Stokes vector using reflection matrices, which is done adequately per surface facet of the asteroid shape model, discussed in Section 1.2. The next step is to make the transition to the instrument's detector. This and other features incorporated in ARM, are discussed in this section.

1.3.1. Interpretation by a detector

After the reflected light from the asteroid has arrived at the observer, it is finally measured by the modeled detector of the instrument. Both to simplify this aspect of ARM and to keep with a realistic design of SPEX, as discussed in Sibbing (2017, Sec. 2.2.1), the modeled detector consists of $n \times n$ squared pixels. The detector is located at the observer's position, $\mathbf{p}_O$, and its horizontal and vertical axes follow the conventions of the y- and z-axes of the planetary scattering plane system. The 2-dimensional detector does not allow for a third dimension, which is why the x-axis of the reference system is ignored and the detector effectively interprets a projection of the planetary scattering plane system in its yz-plane. The horizontal and vertical coordinates of the centers of the pixels are indicated by y_{pixel} and z_{pixel}, respectively.

The algorithm of ARM translating from facets to pixels starts with a double loop over the pixels, covering the horizontal and vertical dimension. Next, a loop over all the facets checks whether the current facet finds its center, $\mathbf{c}_{\text{facet}}$, within the boundaries of the current pixel. See Equation 1.30 and Equation 1.31. Here, Δy_{pixel} and Δz_{pixel} are the width and height of a pixel, respectively.

$$y_{\text{pixel}} - \frac{1}{2}\Delta y_{\text{pixel}} \leq c_{\text{facet},y} < y_{\text{pixel}} + \frac{1}{2}\Delta y_{\text{pixel}} \tag{1.30}$$

$$z_{\text{pixel}} - \frac{1}{2}\Delta z_{\text{pixel}} \leq c_{\text{facet},z} < z_{\text{pixel}} + \frac{1}{2}\Delta z_{\text{pixel}} \tag{1.31}$$

Various parameters are kept track of during the algorithm and are checked afterwards to ensure that all the facets are divided over the detector: the total number of pixels that are non-empty, a list of indexed pixels that are non-empty, a list of indexed facets per pixel, the total number of facets per pixel and the total projected area of facets falling on a pixel. These parameters can be used to determine the Stokes elements F, Q, U and V for a pixel by summing the Stokes elements of the facets falling within that pixel. See Equation 1.32.

$$\pi\mathbf{F}_{\text{pixel}}(m) = \sum_{\text{facets } n \text{ per pixel } m} \pi\mathbf{F}_{\text{facet}}(n) \tag{1.32}$$

The degree and direction of polarization per pixel, P_{pixel} and χ_{pixel}, can be calculated next using Equation 1.3 and Equation 1.7 for $\pi\mathbf{F}_{\text{pixel}}(m)$.

In practice, the area which a detector can cover and the related spatial resolution depends on the distance to the object, the aperture of the instrument, the number of pixels used and more instrument-related variables. It is hard to tell what a realistic spatial resolution will be for SPEX, because none of these variables is known in this phase of the design. However, since almost all currently available polarimetry data is spatially unresolved, or disk-integrated, any resolution which shows some resolved features of the asteroid is already an improvement.

Unlike in the case of real observations, there is an optimum for the number of pixels, other than as many as possible, which depends on the number of facets of the shape model. If the resolution is too high, the ability to resolve features will not improve any further. Instead, the discrete difference between i or $i+1$ facets per pixel and the corresponding difference in Stokes elements between pixels will be increasingly visible for adjacent pixels. In its extremity, this effect will lead to only one or two facets per every so many pixels, the rest of them being empty. It becomes clear that the approach of checking the values of $\mathbf{c}_{\text{facet}}$ for each pixel, which is part of the cause of this problem, is not ideal for high spatial resolutions.

Bearing in mind minimizing this discrete difference problem, the spatial resolution needs to be maximized to find an optimal value for the number of pixels along one dimension of the detector, n_{pixel}. In order to solve this two-parameter optimization problem, the facet-to-pixel ratio, f, is introduced. The error for the discrete difference problem is then proportional to $1/f$, so $\epsilon_1 \propto n_{\text{pixel}}^2 / n_{\text{facet}}$. Maximizing the spatial resolution, dictated by n_{pixel}, is translated to minimizing $\epsilon_2 \propto 1/n_{\text{pixel}}$. Hence, if ϵ_1 and ϵ_2 have equal weight, the solution is to find the minimum of the root sum of squares of both. See Equation 1.33.

$$\epsilon_{\text{total}} = \sqrt{\epsilon_1^2 + \epsilon_2^2} = \sqrt{\left(\frac{n_{\text{pixel}}^2}{n_{\text{facet}}}\right)^2 + \left(\frac{1}{n_{\text{pixel}}}\right)^2} \tag{1.33}$$

Finding the minimum through the derivative of Equation 1.33 results in

$$n_{\text{pixel}} = \left(\frac{1}{2} n_{\text{facet}}^2\right)^{1/6} \tag{1.34}$$

where it is important to mention that n_{facet} represents only the number of illuminated facets, not all of them. Equation 1.34 is clearly an indication for the optimum number of pixels and not an exact value because it is not an integer for all values of n_{facet}. This is further discussed in chapter 2, when various number of pixels are used.

1.3.2. Asteroid orientation changes

Without further adjusting it, the asteroid's orientation follows directly from the DAMIT database: all vertices are expressed in the asteroid body reference system from where translations can be made to other reference systems. If one is interested in data from different orientations of the asteroid, it can be rotated using a rotation matrix. The standard rotation matrices for rotations around the x-, y- and z-axes are given in Equation 1.35 to Equation 1.37 (Weisstein, 2018c), where α is the rotation angle.

$$\mathbf{R}_x(\alpha) = \begin{bmatrix} 1 & 0 & 0 \\ 0 & \cos\alpha & \sin\alpha \\ 0 & -\sin\alpha & \cos\alpha \end{bmatrix} \tag{1.35}$$

$$\mathbf{R}_y(\alpha) = \begin{bmatrix} \cos\alpha & 0 & -\sin\alpha \\ 0 & 1 & 0 \\ \sin\alpha & 0 & \cos\alpha \end{bmatrix} \tag{1.36}$$

$$\mathbf{R}_z(\alpha) = \begin{bmatrix} \cos\alpha & \sin\alpha & 0 \\ -\sin\alpha & \cos\alpha & 0 \\ 0 & 0 & 1 \end{bmatrix} \tag{1.37}$$

If various rotations along different axes are desired, rotation matrices can be multiplied in the order from the first rotation on the right to last rotation on the left. See Equation 1.38.

$$\mathbf{R}_{\text{total}} = \mathbf{R}_2(\alpha_2)\mathbf{R}_1(\alpha_1) \tag{1.38}$$

Finally, any vector $\mathbf{v}$ can be rotated from the old reference system to the new reference system using Equation 1.39.

$$\mathbf{v}_{\text{new}} = \mathbf{R}_{\text{total}}\mathbf{v}_{\text{old}} \tag{1.39}$$

To apply this rotation to ARM, parameters $\mathbf{v}_{\text{facet}}$, $\mathbf{c}_{\text{facet}}(n)$ and $\hat{\mathbf{n}}_{\text{facet}}(n)$ have to be rotated to redefine them in the asteroid body reference system.

ARM applies these rotations at the very beginning of the program in such a way that various orientations can be predefined in terms of elevation, $\epsilon_{\text{orientation}}$, and azimuth, $\phi_{\text{orientation}}$, with respect to the initial orientation. Across these different orientation runs, the mean and variance of the pixel-wise Stokes elements are calculated as follows.

$$\pi\mu_{\mathbf{F}} = \frac{1}{n_{\text{orientation}}} \sum_{n_{\text{orientation}}} \pi\mathbf{F}_{\text{pixel}}(m) \tag{1.40}$$

$$(\pi\sigma_{\mathbf{F}})^2 = \frac{1}{n_{\text{orientation}}} \sum_{n_{\text{orientation}}} (\pi\mathbf{F}_{\text{pixel}}(m) - \pi\mu_{\mathbf{F}})^2 \tag{1.41}$$

where $\pi\mu_{\mathbf{F}}$ and $(\pi\sigma_{\mathbf{F}})^2$ are the mean and the variance of the Stokes vector, given per element. The mean values of the degree and direction of polarization can be determined via relations derived from Equation 1.3 and Equation 1.7:

$$P_{\text{total, mean}} = \frac{\sqrt{\mu_Q^2 + \mu_U^2 + \mu_V^2}}{\mu_F} \tag{1.42}$$

$$\tan 2\chi_{\text{mean}} = \frac{\mu_U}{\mu_Q} \tag{1.43}$$

The pixel-wise mean is a relevant parameter, because this would correspond to what the detector can measure during several observations of an asteroid within a period of time of the order of magnitude of the asteroid's rotation.

1.3.3. Disk-integrated Stokes vector elements

To compare results from ARM with real observations, both time averages, as discussed in Section 1.3.2, and disk-integrated values of the Stokes vector, are interesting. Moreover, even the time average of the disk-integrated values can be calculated, to rule out both temporal and spatial extreme values. The equation for the disk-integrated Stokes vector that is used in ARM follows from Equation 1.16.

$$\begin{aligned}\pi\mathbf{F}_{\text{observer, disk}} &= \frac{1}{d^2}\int_A \mu\mu_0\mathbf{R}_1(\mu,\mu_0,\phi-\phi_0)F_0\,dA \\ &\approx \frac{1}{d^2}\sum_{\text{facet } i}\mu_i\mu_{0,i}\mathbf{R}_1(\mu_i,\mu_{0,i},\phi_i-\phi_{0,i})F_{0,i}A_i = \sum_{\text{facet } i}\pi\mathbf{F}_{\text{observer},i}\end{aligned} \tag{1.44}$$

Substituting the result from Equation 1.44 into Equation 1.40 and Equation 1.41 gives the orientation average of the disk-integrated values of the Stokes vector and its associated variance.

2

ARM verification

In this chapter, the verification of is found in is discussed. To verify the correctness of output variables such as the Stokes elements, the degree and direction of polarization and important angles such as rotation angle β from Equation 1.6 and azimuthal angle $\phi - \phi_0$, a spherical polyhedron model consisting of 8,192 facets is used. This model was generated using a sphere generation algorithm from Bourke (1992). The algorithm allows for the choice of an exponent such that the total number of facets is $8 \cdot 4^n$. Hence, 512, 2,048 and 8,192 facets are logical choices in comparison to the number of facets of the available asteroid shape models. For the sake of accuracy, the latter was chosen and is used throughout this section. Table 2.1 shows an overview of is found in verification tests that will be discussed hereafter.

Table 2.1: Overview of is found in verification tests that have been performed specifying the shape model, the surface scattering model, the used phase angle(s) and the parameter(s) specified by the color of each of the associated figures.

#	**Shape model**	**Surface scattering model**	**Phase angle(s)**	**Parameter(s)**
1	Sphere	Lambertian reflection	0°, 45°	F
2	Sphere	*Independent*	0°, 45°	β, $\phi - \phi_0$
3	Sphere	Lambertian reflection	0°, 45°	F_{pixel}
4	Sphere	martian analog	0°	F, Q, U, P_{total}, χ
5	(216) Kleopatra	martian analog	0°	F, P_{total}, $\phi_{\text{orientation}}$

2.1. Model fundamentals

2.1.1. Shape model and radiation flux

The first verification test amounts testing the shape model, the radiation flux, F, and the effect of different phase angles, α. The surface scattering model that is used here is Lambertian reflection, which does not allow for polarization effects. Hence, Stokes elements Q, U and V as well as the degree of polarization P_{total} are all zero. The Lambertian scattering model has a surface albedo of $A = 0.20$ and consists of 31 Gaussian abscissae, including the added abscissa at opposition. Figure 2.1 depicts the unscaled radiation flux for values of $\alpha = 0°$ (*left*) and $\alpha = 45°$ (*right*). Recall that the planetary scattering plane system has its x-axis coincide with the asteroid-observer direction, which is the viewer direction in all figures from now on. In (*right*), the asteroid-Sun vector is directed to the right-hand side.

The pattern for the flux is as expected: the effect of μ_0 and μ is dominant and creates a maximum on the sphere between the observer direction and the Sun direction (which coincide in Figure 2.1 (*left*)). More precisely, the product $\mu_0\mu$ from Equation 1.15 dictates the portion of the flux arriving at the observer, which explains both the maxima in the center and the minima near the edge in Figure 2.1 (*left* and *right*). Note that (*left*) is point-symmetric around the center and (*right*) is plane-symmetric in xz-plane. For the latter figure,

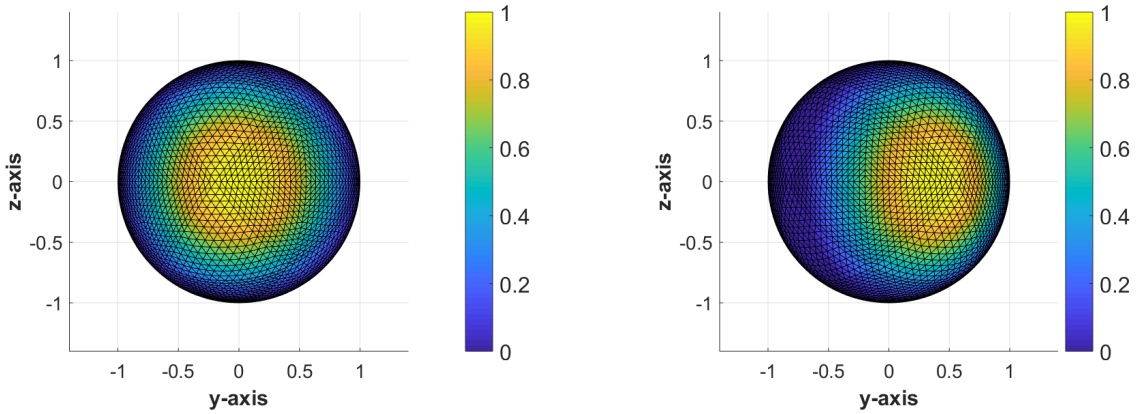

Figure 2.1: The spherical shape model in the planetary scattering plane system as seen with zero phase angle (*left*) and 45° phase angle (*right*). The colors represent the unscaled Stokes element F. The surface scattering model is the model for Lambertian reflection.

this includes the zero-value crescent on the left, which indicates that in that area, either $\mu_0 < 0$ or $\mu < 0$ or the area suffers from self-shading.

2.1.2. Azimuthal and reference frame angles

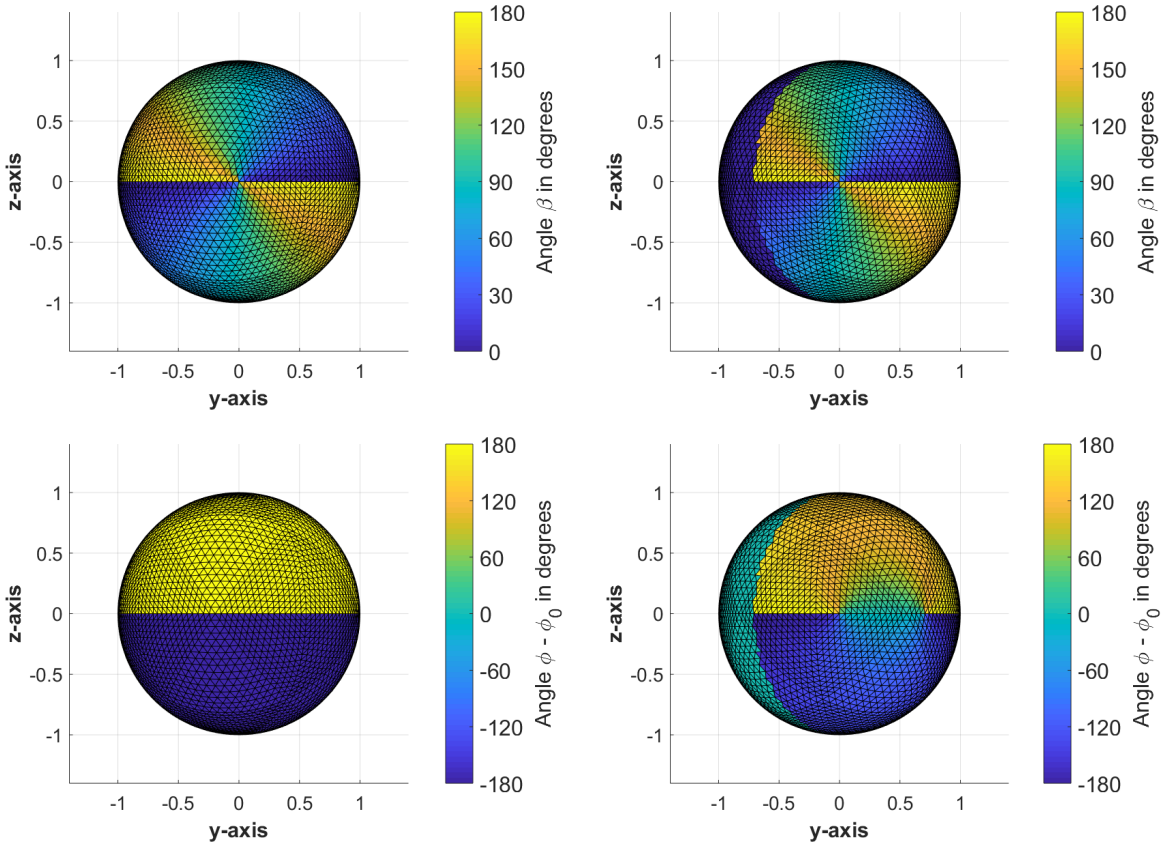

Figure 2.2: *Top*: rotation angle β as occurred before in Equation 1.6, shown per facet in the planetary scattering plane system, evaluated with zero phase angle (*left*) and 45° phase angle (*right*). *Bottom*: azimuthal angle $\phi - \phi_0$ as is discussed in Section 1.1.3, evaluated with zero phase angle (*left*) and 45° phase angle (*right*). The zero-value crescent on the left in the two right-hand side figures represents an area on the sphere that is not illuminated. The patterns for β and $\phi - \phi_0$ are independent of the surface scattering model.

The second verification test checks the definitions of the rotation angle, β, which rotates from the local merid-

ian plane system to the planetary scattering plane system, and of the azimuthal angle, $\phi - \phi_0$, both of which are fundamental for the correct values of P_{total} later on. Since these angles are independent of the surface scattering model, they can already be tested during a simulation with the Lambertian reflection scattering model. Plots for β and $\phi - \phi_0$ (*top*, *bottom*) for 0° and 45° phase angle (*left*, *right*) are shown in Figure 2.2.

By definition, β is the angle between the local meridian plane and the planetary scattering plane, rotating clockwise as seen from the observer's position. Since the planetary scattering plane is an ambiguous phenomenon when $\alpha = 0°$, it is defined as if the phase angle is infinitesimally small and $\hat{\mathbf{r}}_{\text{AS}}$ lies in the positive y-direction. This keeps the definition of the planetary scattering plane and the behavior of β consistent with cases where the phase angle is non-zero.

The azimuthal angle $\phi - \phi_0$ is by definition 180° minus the angle between plane of incidence and plane of reflection, again rotating clockwise as seen by the observer. As is shown in Figure 2.2 (*bottom right*), $\phi - \phi_0$ is zero or ±180° at the equator, positive in the northern hemisphere and negative in the southern hemisphere, due to the convention of clockwise rotation. In follow-up verification tests, it will be shown that the degree of polarization behaves as expected using these conventions for β and $\phi - \phi_0$.

2.1.3. Detector view

The third verification test considers the detector view of the spherical shape model, while varying the number of pixels. All input parameters of the model are identical to the ones used in the first verification test, of which the results were shown in Figure 2.1. In Section 1.3.1, it was discussed that there exists an optimal facet-to pixel ratio for the detector. Deviating too much from this optimum results in very bad spatial resolution (too few pixels) or a large portion of the pixels left empty (too many pixels). It appears that there is yet another effect which dictates the optimal number of pixels: the pattern in the positions of the facets. Both effects are

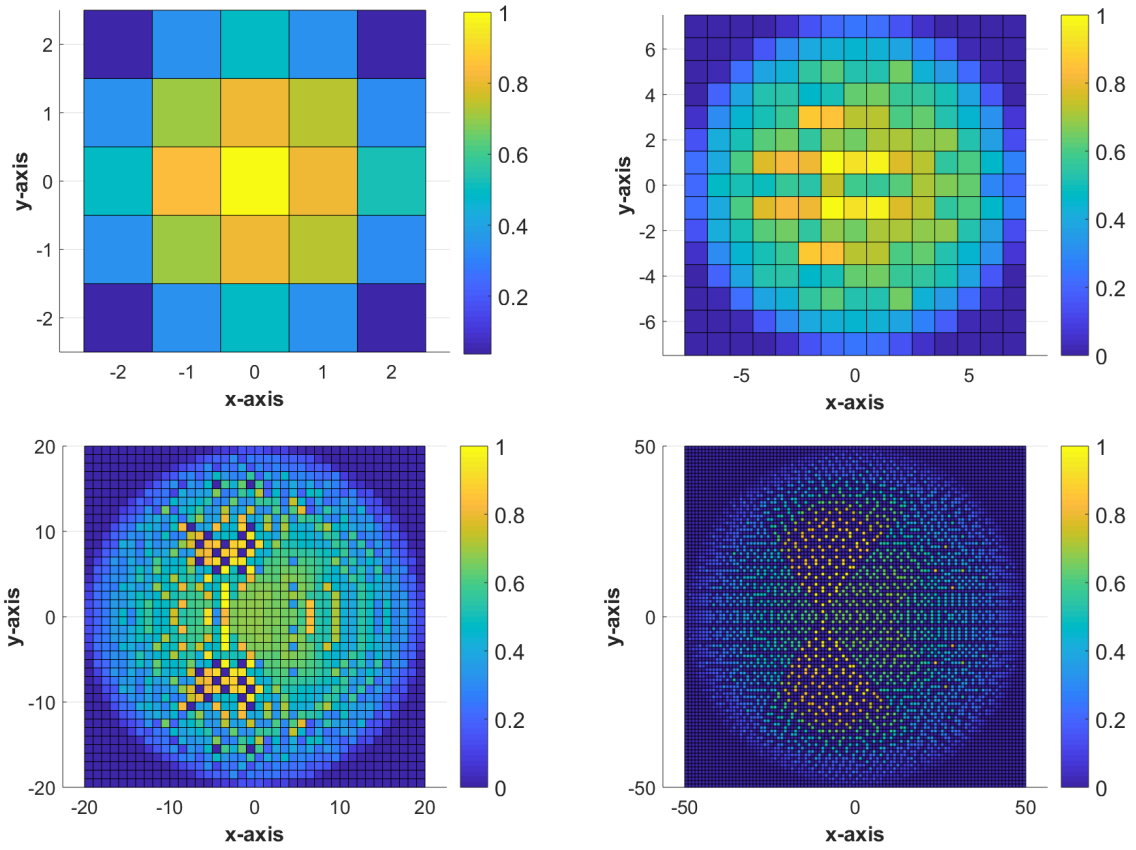

Figure 2.3: Four examples of non-ideal representations of a detector view of Figure 2.1 (*left*), using various numbers of pixels along one dimension: $n_{\text{pixel}} = 5, 15, 40, 100$, (*top left*, *top right*, etc.). Associated facet-to-pixel ratios are $f = 164, 18.2, 2.56, 0.410$, respectively.

shown in Figure 2.3.

Figure 2.3 shows four examples of non-ideal choices for the amount of pixels: $n_{\text{pixel}} = 5, 15, 40, 100$. The $n_{\text{pixel}} = 5$ pixel detector (*top left*) has facet-to-pixel ratio $f = 4,096/25 = 164$, when only illuminated facets are considered. This results in a very coarse spatial resolution and it can hardly be concluded that the observed object is actually a sphere. The $n_{\text{pixel}} = 15$ pixel detector (*top right*) shows a better spatial resolution but has some peculiar horizontal features across four different rows of pixels. These lines are caused by the pattern of the facets (see Figure 2.1) on the sphere, an effect which is unavoidable because the pattern on the sphere is constant everywhere. This problem will not occur when using an (irregular) asteroid shape model. The $n_{\text{pixel}} = 40$ and $n_{\text{pixel}} = 100$ detectors (*bottom*) have $f = 2.56$ and $f = 0.410$, respectively. These are values for which increasing numbers of pixels will be completely empty and the discrete difference between 1, 2 or 3 facets per pixel is dominant over the individual flux contributions of the facets. Both effects make these detector simulations useless.

In Equation 1.34, a theoretically supported optimal value for n_{pixel} was given. The equation is repeated here for convenience. The problem with the horizontal features of Figure 2.3 (*top right*) is ignored for reasons mentioned before.

$$n_{\text{pixel}} = \left(\frac{1}{2} n_{\text{facet}}^2\right)^{1/6} \tag{2.1}$$

Evaluating this equation for $n_{\text{facet}} = 4,096$ gives $n_{\text{pixel}} \approx 14$. The detector view with $n_{\text{pixel}} = 15$, shown in Figure 2.3 (*top right*) thus is close to ideal according to Equation 2.1. It is unfortunate that the undesired horizontal features ruin the quality of the image.

Now that $n_{\text{pixel}} = 14$ is available as an initial guess, a solution without the horizontal stripes should be close. Figure 2.4 shows detector views with $n_{\text{pixel}} = 10$, for phase angles zero (*left*) and 45° (*right*), resulting in facet-to-pixel ratios of $f = 41.0$ and $f = 31.6$, respectively. From Figure 2.4 (*left*) it can be concluded that the observed object has a circular or almost circular projection given the current orientation. In practice, if more images of different orientations could be captured, the object might turn out to be spherical or almost spherical. A similar hypothetical analysis can be performed on Figure 2.4 (*right*), taking into account the phase angle.

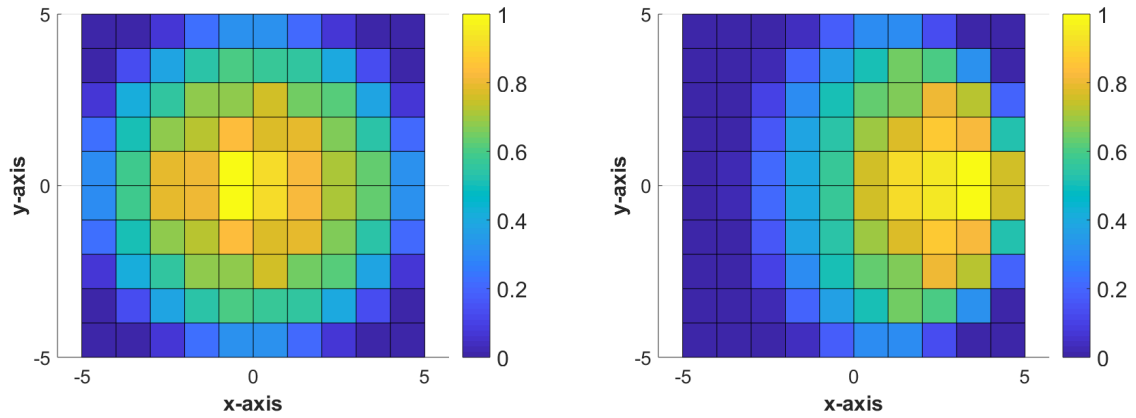

Figure 2.4: Two detector view representations of Figure 2.1 where phase angles are $\alpha = 0°$ (*left*) and $\alpha = 45°$ (*right*) and $n_{\text{pixel}} = 10$ for both. This value for n_{pixel} is close to the optimal value of $n_{\text{pixel}} = 14$, derived from Equation 2.1.

2.2. Polarization

2.2.1. Stokes elements and polarization

The fourth verification test introduces a different surface scattering model than the model for Lambertian reflection, namely the martian analog model. This model does not ignore Q and U any longer and generates polarization as a result. Unfortunately for the negative polarization, coherent backscattering and shadow hiding are not accounted for in this model. Due to the absence of these effects, the resulting polarization pattern

has more similarities with a gaseous planet's polarization pattern than an asteroid's. However, for verification means, this is not important. The scattering matrix elements are provided by the Amsterdam Light Scattering Database (Muñoz et al., 2012; Volten et al., 2012) under the name 'martian analog (palagonite)' (Laan et al., 2009).

Where the number of Gaussian abscissae was not an important parameter in the Lambertian scattering model, it is for the martian analog. Fewer abscissae will result in coarser interpolations between values of μ and μ_0, thus harming the accuracy of the simulation. On the other hand, too many Gaussian abscissae will increase the computational effort quadratically. Several numbers of abscissae, n_{abscissa}, are tested for their resulting accuracy within the framework of this verification test.

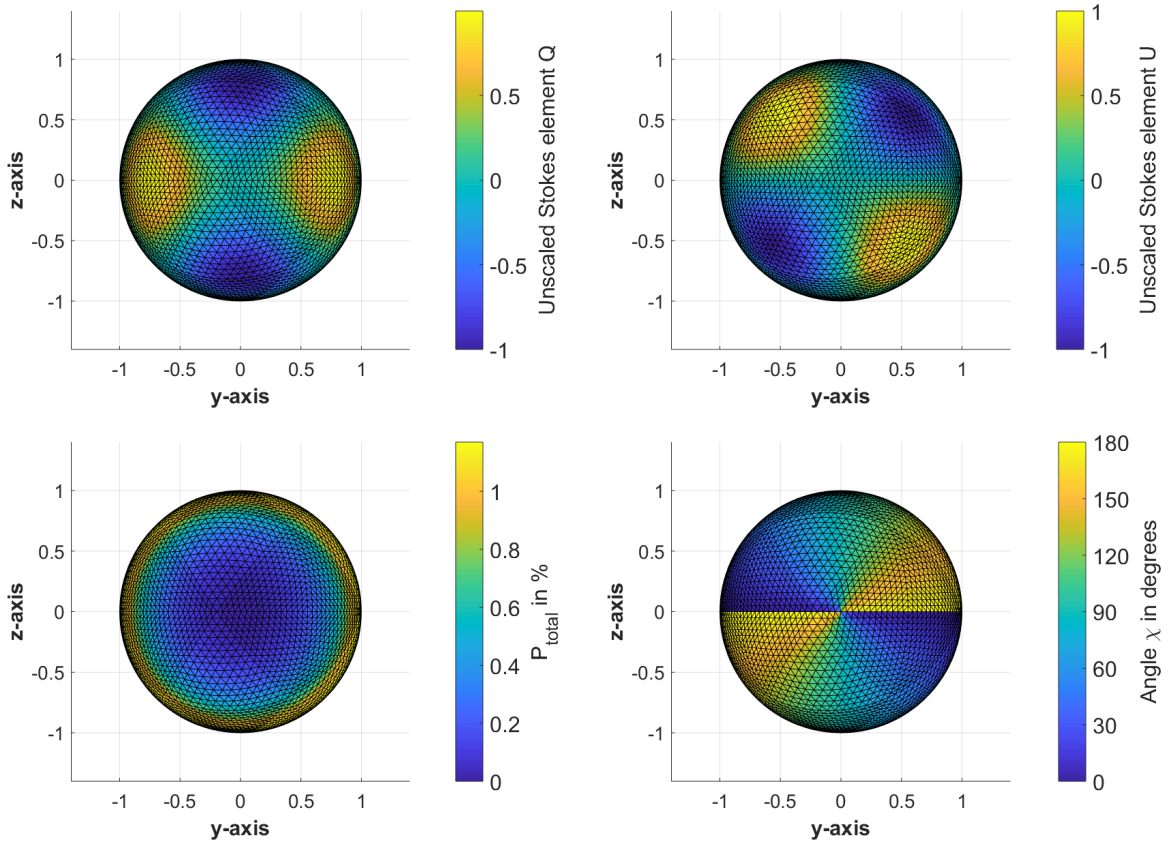

Figure 2.5: Stokes elements Q (*top left*) and U (*top right*), the degree of polarization, P_{total}, (*bottom left*) and the direction of polarization, χ, (*bottom right*), using the martian analog model and $\alpha = 0°$. The number of Gaussian abscissae is 60.

Figure 2.5 depicts the Stokes elements Q and U and the degree and direction of polarization, P_{total} and χ, respectively. The unscaled flux has a pattern identical to the flux with Lambertian reflection, shown in Figure 2.1 (*left*), therefore it is not repeated here. The patterns for Q and U are largely symmetrical along the y- and z-axes (Q) and along $y = z$ and $y = -z$ lines (U), which is understandable for a sphere. The polarization, as a result, is rotationally symmetric and has a minimum in the center. There the flux is highest and Q and U are low which makes the degree of polarization vanish according to Equation 1.3. The maximum values near the edge of Figure 2.5 (*bottom left*) correspond to polarization behavior of gaseous planetary atmospheres such as Jupiter's (Dollfus, 1957; Schmid et al., 2011). For asteroids, there is no concrete knowledge of this effect. Disk-integrated values for Q, U and P_{total} all equal zero due to the symmetry. The direction of polarization shown in Figure 2.5 (*bottom right*) supports this, for it indicates that for each facet, the polarization lies in the radial direction in the yz-plane. The number of Gaussian abscissae used in this simulation was 61, including one added abscissa at opposition.

As has been mentioned before, too few Gaussian abscissae will harm the accuracy of the Fourier coefficients, $\mathbf{R}_1^m(\mu, \mu_0)$, used in determining the reflection matrix $\mathbf{R}_1(\mu, \mu_0, \phi - \phi_0)$. Through trial-and-error, it was found

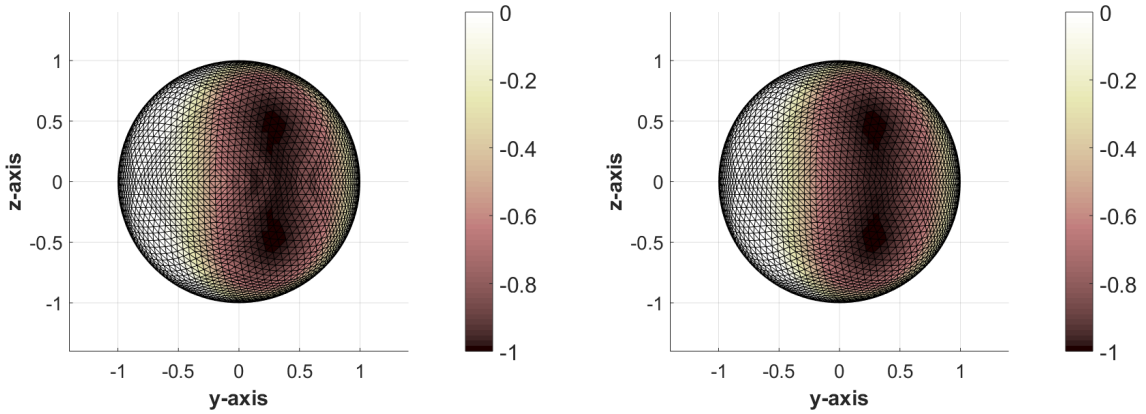

Figure 2.6: Plots of Stokes element Q simulated using $\alpha = 45°$ and different numbers of Gaussian abscissae in calculating the Fourier coefficients: 20 (*left*) and 80 (*right*). The left plot has unwanted circular features around the Sun direction and observer direction.

that at least 60 Gaussian abscissae is enough to suppress unwanted features in the figures for P_{total}, as shown in Figure 2.5. However, more abscissae will increase the accuracy further. Figure 2.6 depicts two different plots of Stokes element Q with $\alpha = 45°$, using only 20 abscissae (*left*) and as much as 80 abscissae (*right*). The color scheme is different from the one used before, to indicate the alternating features near $\mu_0 = 1$ and $\mu = 1$ better. The circular features only occur at up to about 40 Gaussian abscissae and are caused by coarse interpolation between values of μ and μ_0. Obviously, if and where this behavior occurs, is specific to the surface scattering model, for each model has its own relations for $\mathbf{R}_1(\mu, \mu_0, \phi - \phi_0)$. In the current situation, apparently the number of abscissae between $\mu, \mu_0 = 0.9$ and $\mu, \mu_0 = 1$ is insufficient although the spacing between abscissae is already highest there following the Gaussian distribution. The result is that Q, U and P_{total} all have circular features around $\mu, \mu_0 = 1$.

2.2.2. Asteroid polyhedron model

The fifth verification test finally uses an asteroid polyhedron model instead of the spherical model which is only meant for verification purposes. The goal of this verification is to assess the effect of different orienta-

Table 2.2: Summary and conclusions of the five performed verifications as given in Table 2.1.

#	**Conclusion**
1	The polyhedron model functions correctly and the evaluation of F using a simple Lambertian scattering model with various phase angles, is as expected. Each facet's individual parameters, as were introduced in Table 1.1 are calculated correctly.
2	Important angles β and $\phi - \phi_0$ are evaluated correctly according to their definitions and behave as expected under different phase angles.
3	Detector views are often not very accurate as soon as the number of pixels deviates a lot from the optimal number given in Equation 2.1. However, ideal or near-ideal numbers of pixels do result in a representative detector image, based upon which some conclusions can be drawn with respect to the observed object.
4	It was verified that the martian analog scattering model generates values for Stokes elements Q and U and the degree of polarization P_{total}. The polarization pattern of having low values in the center and higher values at the edge were recognized as globally resembling the polarization pattern of a gaseous planet such as Jupiter (Dollfus, 1957; Schmid et al., 2011). Furthermore, the effect of different numbers of Gaussian abscissae was discussed. Depending on the desired accuracy of Q and U, a minimum number of abscissae should be used in the simulations.
5	The asteroid polyhedron model of Kleopatra gives the expected results for all Stokes elements and the degree of polarization. is found in assesses self-shading correctly and indeed neglects non-illuminated facets. Also, changing the orientation of the asteroid over sequential simulations, works.

tions of the shape model on the flux and degree of polarization and evaluate self-shading in these orientations. Here, again, the martian analog scattering model is used. The phase angle is $\alpha = 45°$ with the position of the Sun in the right-hand side of the plot, in order for self-shading to occur. Figure 2.7 (*top* to *bottom*)depicts asteroid (216) Kleopatra in three different orientations, where the orientation azimuth, $\phi_{\text{orientation}}$, equals 0°, 36° and 72° and the orientation elevation remains constant. Colors represent the unscaled flux (*left*) and the degree of polarization (*right*). The large dark areas on the left-hand side of Figure 2.7 (*top*) indicate that those facets are not illuminated at all, due to failing at least one of the four requirements of the self-shading algorithm, discussed in Section 1.2.2. Especially the area on the top side of the asteroid in Figure 2.7 (*top*) experiences self-shading of the large hump on the right-hand side, as has been verified by assessing the different steps of the self-shading algorithm. Note that the shaded area occurred before, in Figure 2.1 (*right*), where the phase angle was 45° as well. Despite this, the role of the shape model and the orientation apparently is more dominant than the role of the phase angle, in the case of Kleopatra, which can be concluded from the significant differences between flux plots in Figure 2.7 (*left*). The reason for both effects is that the distribution of μ_0 and μ values across the asteroid's surface is far from uniform such as with the sphere.

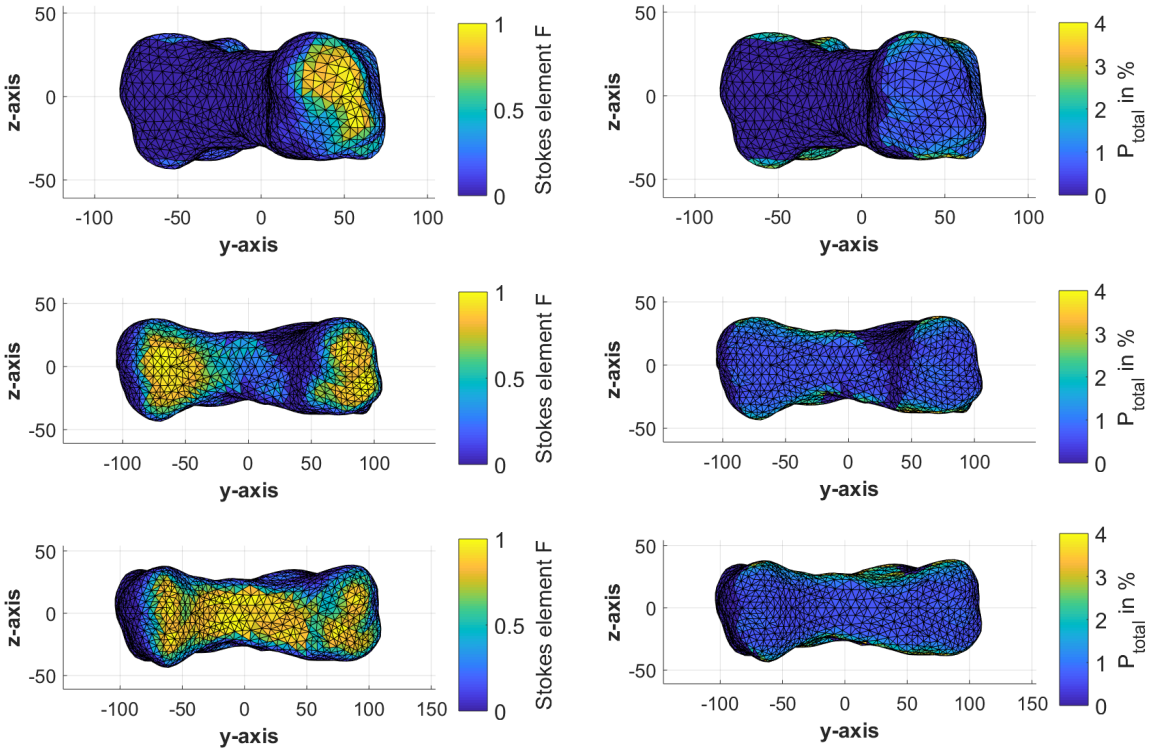

Figure 2.7: Plots for the flux (*left*) and the degree of polarization (*right*) as seen on asteroid (216) Kleopatra using $\alpha = 45°$ and three different orientations. The asteroid polyhedron model originates from the Small Body Radar Shape Models database of the Planetary Data System (Ostro et al., 2004; Neese, 2004). The azimuth angles of the orientations, $\phi_{\text{orientation}}$, are 0°, 36° and 72° (*top* to *bottom*).

Practically all the functionalities and output parameters of is found in have been verified at this point. Table 2.2 gives an overview of the conclusions that can be drawn based upon these past verifications. What remains is the validation of disk-integrated Stokes elements and polarization values with available polarimetric data. This is one of the topics of Section 3.3.

3

ARM results and application

In this chapter, all kinds of results as generated with ARM are discussed, using different surface scattering models that have not been presented so far. Associated results will be evaluated and compared with one another. In chapter 2, only spatially resolved results were presented as means of verification, not disk-integrated results. One would like to generate disk-integrated phase-polarization plots as well, because this relation is commonly found in databases for historical polarimetric observations of asteroids. Comparing phase-polarization plots of historical observations with ARM-generated phase-polarization plots is a promising way of validating a certain surface scattering model for it to fit to a certain asteroid's surface. Spatially resolved results and phase-polarization curves are assessed in Section 3.2 and Section 3.3, respectively. First, various surface scattering models are discussed in Section 3.1 and the choices for them are supported adequately.

3.1. Realistic surface scattering models

To generate realistic surface scattering models, multiple sources can be used that contain data which finally result in Fourier expansions serving as input for ARM (see Section 1.1.3, the program that produces the Fourier expansions is referred to as Fourier Series Program). Sources for scattering matrix elements of specific materials are the Amsterdam Light Scattering Database (Muñoz et al., 2012; Volten et al., 2012), which is where the martian analog data originates from, and the Granada Light Scattering Database (Muñoz et al., 2012; Muñoz, 2018). Both databases are operated by a cooperation of people from two institutes, hence the Amsterdam-Granada database. Another method is to calculate the scattering matrix elements of a certain sample using the SIRIS program (Muinonen and Nousiainen, 2003), of which the use and functionalities will be discussed shortly. Using one of these sources, the scattering matrix elements can be converted to scattering coefficients which can in turn be used as input for the Fourier Series Program. To balance accuracy and computational effort, the number of Gaussian abscissae that is used in the Fourier Series Program, is 60 for all materials discussed below.

Table 3.1: An overview of SIRIS input parameters and the associated materials the parameters are based on. All particle sizes are 100 μm.

#	**Material**	**Wavelength (λ)**	**Size parameter (x)**	**Refractive index (m)**
1	Artificial	628.3 nm (Red)	1000.0	$1.3000 + i9.9 \cdot 10^{-3}$
2	Artificial	628.3 nm (Red)	1000.0	$1.5000 + i9.9 \cdot 10^{-3}$
3	Artificial	628.3 nm (Red)	1000.0	$1.7000 + i9.9 \cdot 10^{-3}$
4	Hematite	435.3 nm (Blue)	1443.4	$2.7387 + i0.9628$
5	Hematite	547.7 nm (Visible)	1147.2	$2.9210 + i0.4674$
6	Hematite	634.9 nm (Red)	989.6	$2.7877 + i0.1146$
7	Hematite	879.7 nm (Infrared)	714.2	$2.5491 + i0.05703$
8	Olivine	628.3 nm (Red)	1000.0	$1.6200 + i1.0 \cdot 10^{-5}$

The SIRIS program can be used conveniently to simulate light scattering by a sample of particles of a certain shape and size. The program's algorithm is based on Monte Carlo ray-tracing ray optics. The number of parameters to be set in order to simulate the desired sample is quite extensive. For a single particle, these include the radiation wavelength, λ, the refractive index, m, the particle size distribution (radius' mean and standard deviation), the areal fraction of Lambertian diffusion and settings for the shape of the particle. For the sample as a whole, parameters include the number of particles, the number of radiation rays, the accuracy of the ray tracing, the number of the scattering angles, the accuracy of the scattering and azimuthal angles, and more. Here, only the particle settings were adjusted but the sample settings were constant. Finally, SIRIS uses two different bases for the particle shape: Gaussian random sphere geometry and randomly oriented polyhedral particles. Here, the first option was used. Table 3.1 gives an overview of the particle input parameters that were used and the associated materials based upon which the parameters were chosen. The wavelength and

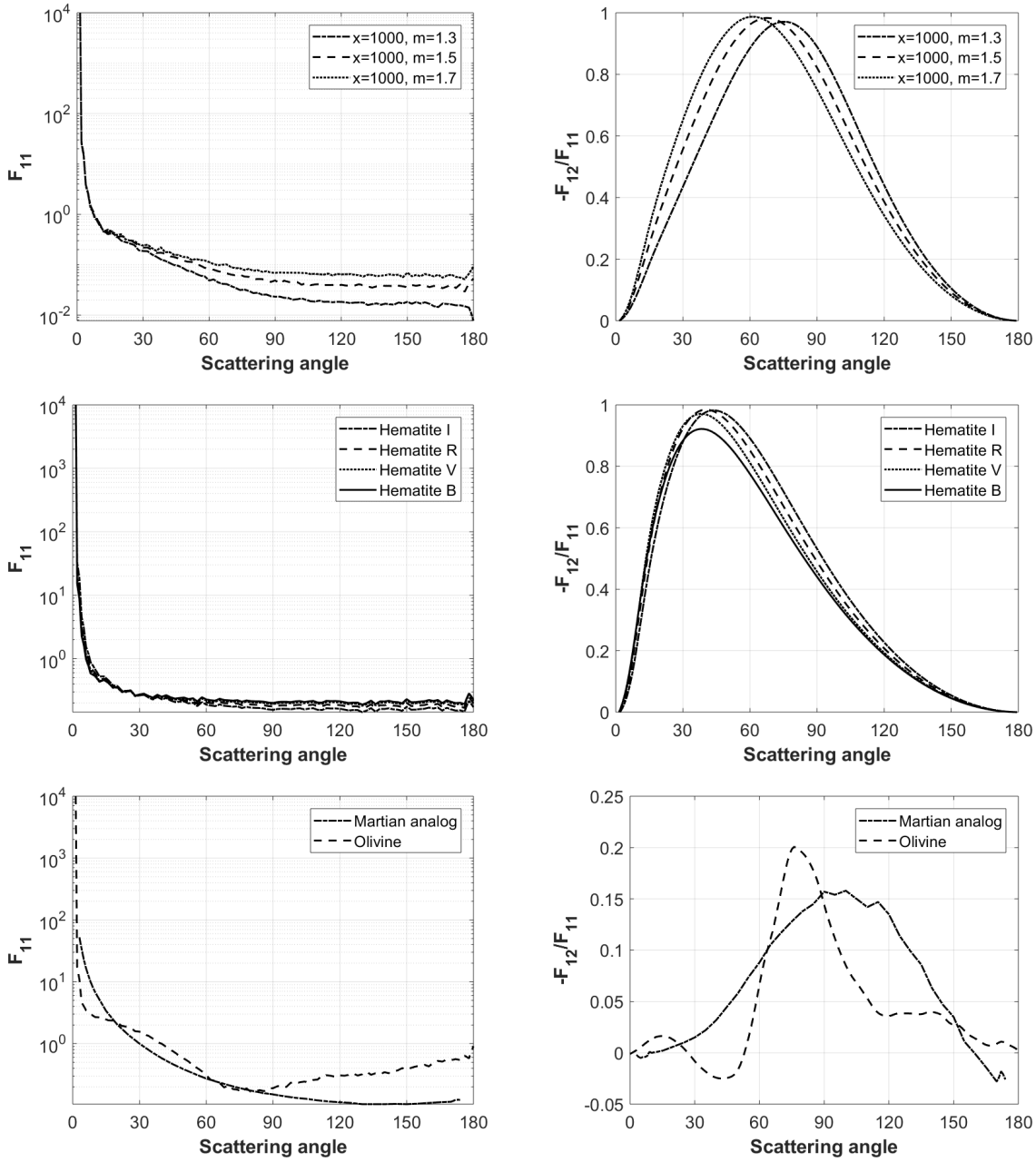

Figure 3.1: Single scattering elements of the artificial materials (*top*), hematite variants for various wavelengths (*middle*) and the martian analog and olivine (*bottom*). Details are given in Table 3.1.

the size parameter are coupled through the relation $x = \frac{2\pi r}{\lambda}$ where r is the mean particle radius. The mean particle radius is indeed set to 100 μm, which results in the values for x as given here. The output in terms of scattering matrix elements F_{11} and $-F_{12}/F_{11}$ of these materials is depicted in Figure 3.1, where F_{11} and F_{12} are elements (1,1) and (1,2) of Equation 1.18, respectively. The depicted (relative) elements F_{11} and $-F_{12}/F_{11}$ are generated by SIRIS and smoothed with a linear interpolation function (MATLAB, 2018a) and a smoothing spline function (MATLAB, 2018b), respectively. Exceptions are the martian analog elements, which originate from the Amsterdam Light Scattering Database and are used unaltered.

There is a multitude of reasons for the specific set of materials in Table 3.1. First, the Amsterdam Light Scattering Database has an aerosol section in which the martian analog, hematite and olivine are included, which makes the scattering matrices for these materials easily accessible. Hematite is known for its extreme refractive index, which varies strongly with wavelength, making it an interesting example to use if the effect of wavelength on the degree of polarization is to be investigated. Second, an extraordinary high degree of polarization is observed for asteroid (3200) Phaethon (discussed in Section 3.4), values that a hematite sample with a large x could match, judging from Figure 3.1 (*middle right*). Even higher degrees of polarization are met through using artificial materials with a range of refractive indices around $m = 1.5000 + i9.9 \cdot 10^{-3}$ and a size parameter of at least $x = 1000$ (Escobar-Cerezo, 2018). Single scattering F_{12} elements such as depicted in Figure 3.1 (*top right*) and (*middle right*) typically give high degrees of polarization: the farther to the right the peak is located, the higher the overall expected polarization is. In his thesis, Escobar-Cerezo distinguishes highly absorbing ($m = 1.5000 + i9.9 \cdot 10^{-3}$) and weakly absorbing ($m = 1.5000 + i9.9 \cdot 10^{-5}$) particles (also varying in x for both) of which the first one results in an overall higher degree of polarization. Olivine loosely represents the weakly absorbing particle here, with scattering matrix element $-F_{12}/F_{11}$ of the same order of magnitude as the martian analog's, see Figure 3.1 (*bottom right*). Because the olivine polarization is not high enough to fit to Phaethon's data, it is only used as an illustration of weakly absorbing particles here.

3.2. Spatially resolved results

In Section 2.2, the final verification covered the martian analog-covered shape model of asteroid (216) Kleopatra in three different orientations, showing flux and degree of polarization behavior. The hypothesis is that this scattering model does not match with an asteroid's, which one would like to confirm during the validation of the output results of ARM. The type of asteroid polarimetry data with respect to which validation could be done, is a phase-polarization curve for a target asteroid, for which sources with vast amounts of data exist. This is the topic of Section 3.3. Here, spatially resolved results of ARM are discussed, for various asteroids that are candidates for validation.

Trivial choices for validation asteroids are asteroid for which significant validation data is available. In simulations with ARM, the range of phase angles per asteroid is tailored to the available validation data phase angles. The asteroids used for this validation are (7) Iris, (4) Vesta, (216) Kleopatra and (25143) Itokawa because for three out of four of these asteroids, many polarimetric observations are available in the Asteroid Polarimetric Database (APD). The last one, Kleopatra, was originally chosen for its peculiar shape and associated self-shading and it is continued to be used for this reason. The polyhedron model for Iris is found in the DAMIT database (Ďurech et al., 2010; Ďurech, 2018), Vesta is found in the Small Body Optical Shape Models database of the Planetary Data System (PDS) (NASA, 2018; Thomas et al., 1997), Kleopatra is found in the Small Body Radar Shape Models database of the PDS (Ostro et al., 2000, 2004) and Itokawa is found in the Gaskell Itokawa Shape Model library (Gaskell et al., 2008), although Itokawa is also available in the Small Body Radar Shape Models database. However, the latter shape model originates from observations acquired before the Hayabusa mission (which is where the Gaskell Itokawa Shape Model library originates from) and thus is obsolete. The format for the Vesta model is (*latitude*, *longitude*, *radius*) so the translation to (*vertices*, *facets*) had to be made using a custom MATLAB® script. The shapes of these four asteroids are shown in Figure 3.2. Regarding the surface scattering model used with the four aforementioned asteroids, only the martian analog is used, although the results that can be generated using this model are limited. The materials and associated scattering models that were discussed in Section 3.1 are used only with asteroid (3200) Phaethon for reasons discussed in Section 3.4.

Degree of polarization patterns across asteroids Iris, Vesta and Itokawa are shown in Figure 3.3 for two phase angles each. Polarization patterns for Kleopatra were already shown in Figure 2.7 for a 45° phase angle and

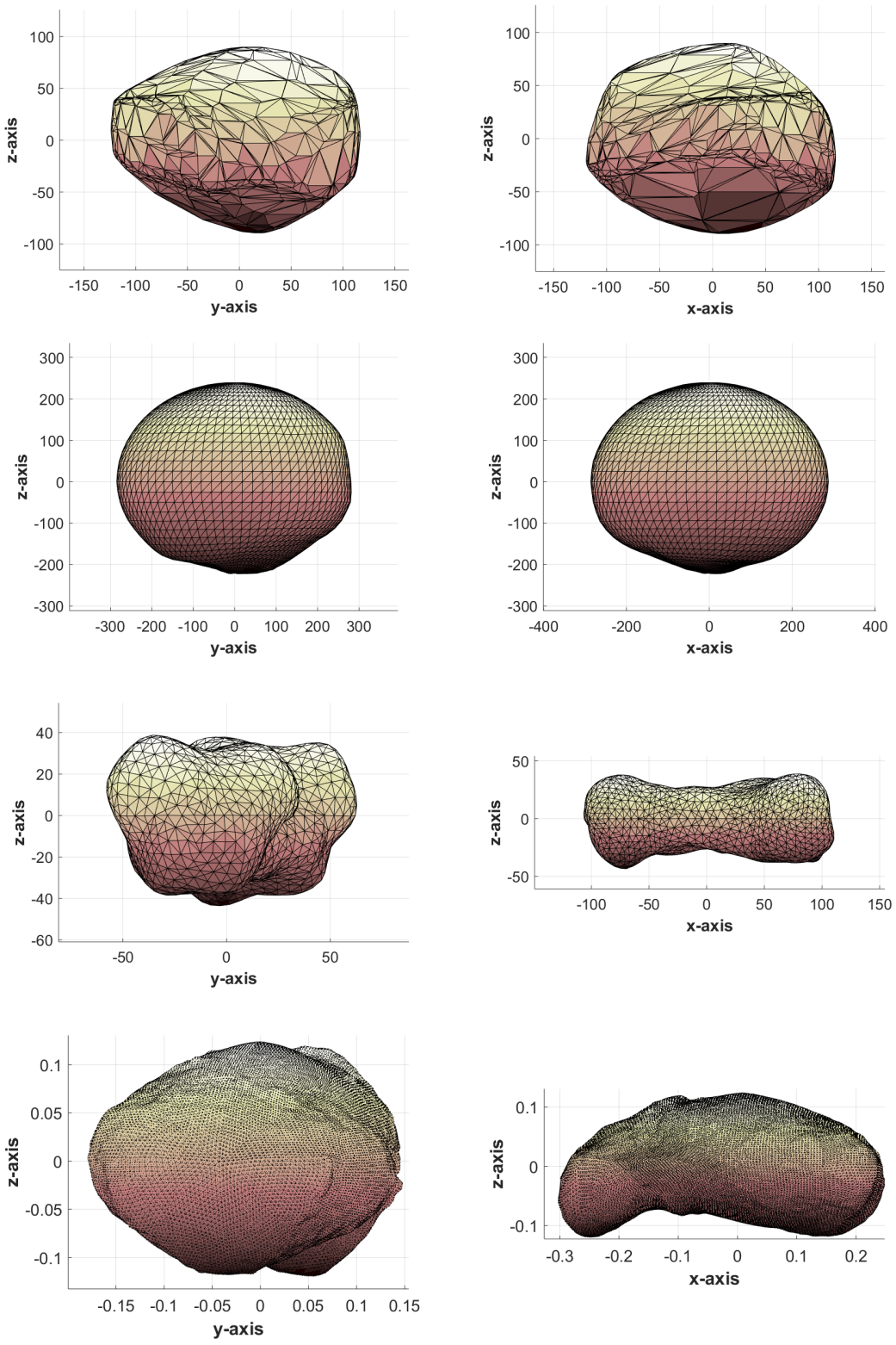

Figure 3.2: Polyhedron shape models of asteroids (7) Iris, (4) Vesta, (216) Kleopatra and (25143) Itokawa (*top* to *bottom*), as viewed with $\phi_{\text{orientation}} = 0°$ (*left*) and $\phi_{\text{orientation}} = 90°$ (*right*). The number of facets per polyhedron are (*top* to *bottom*) $n_{\text{facet}} = \{2{,}040;\ 5{,}184;\ 4{,}092;\ 49{,}152\}$. The units of the axes are [km], revealing that Itokawa is indeed three orders of magnitude smaller than the other three.

various asteroid orientations. Here, instead, the phase angle varies and the orientation does not, except for a rotation as a result of the phase angle (the orientation is kept constant with respect to the direction to the Sun instead of the observer). The chosen phase angles match phase angles that are found in the polarimetric data, which are 15°, 30° for Iris and Vesta and 50°, 70° for Itokawa. For Kleopatra, there is only one available polarimetric observation which makes it impossible to fit a curve to the data. Polarimetric data for the other three asteroids are discussed in Section 3.3.

Across the three asteroids in Figure 3.3, both similarities and differences can be noted. All show zero degree of polarization values in the center, low values *around* the center and high values near the edge, in a near-circularly symmetric way. Depending on the amount of facets of the polyhedron model, larger or smaller areas are green/orange (for example, *top right* compared to *middle right*). A main difference between aster-

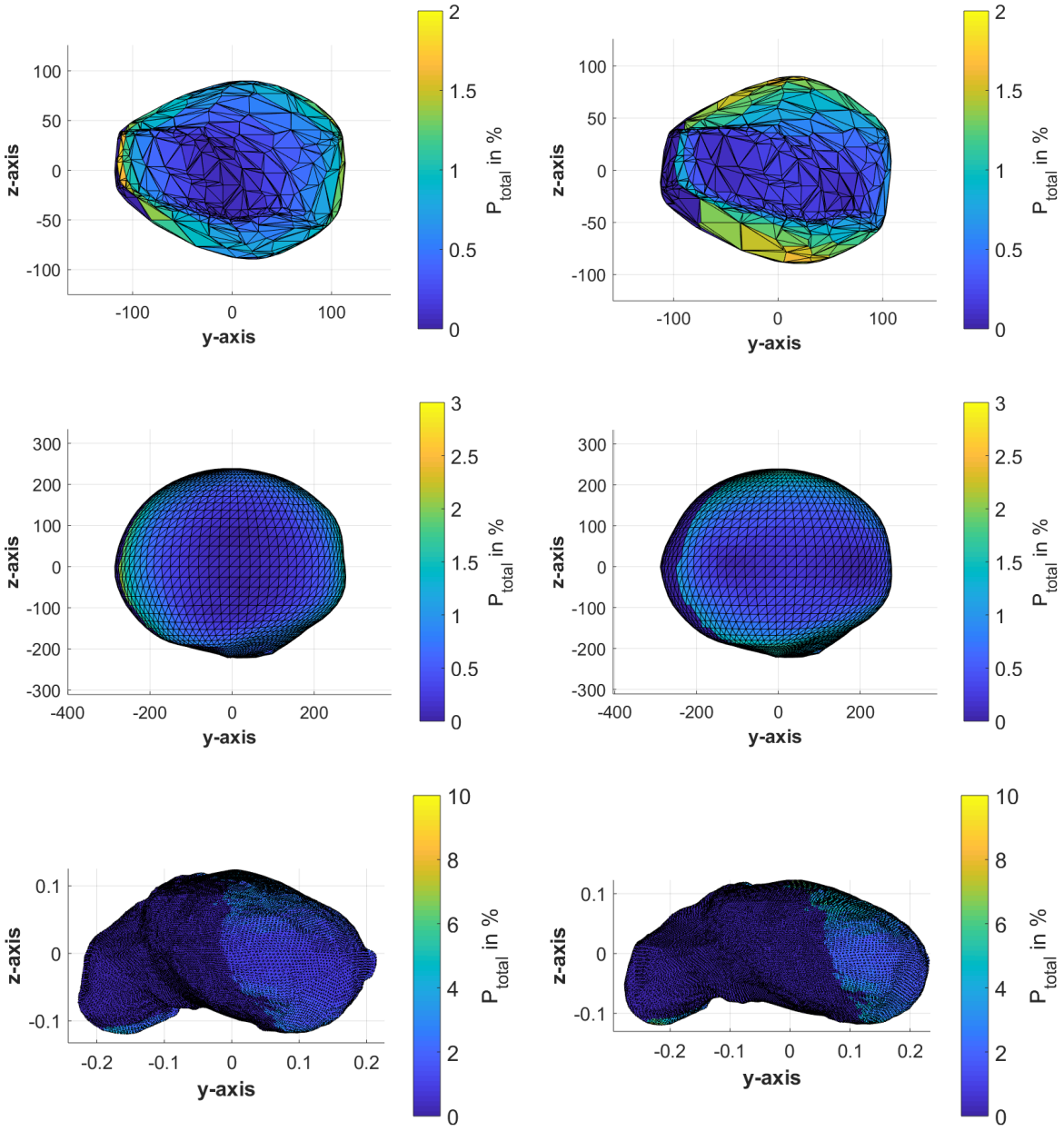

Figure 3.3: Plots for P_1 as seen on the surfaces of asteroid (7) Iris, (4) Vesta and (25143) Itokawa (*top* to *bottom*). Phase angles are (*left* to *right*) 15°, 30° for both Iris and Vesta and 50°, 70° for Itokawa, approximately according to the phase angles for which validation data is available. The surface scattering model is martian analog (Muñoz et al., 2012; Volten et al., 2012).

oids and phase angles is the magnitude of the degree of polarization. Between Iris and Vesta, the polarization scale difference as indicated by the colorbar values gives away that the maximum degree of polarization for a single facet is higher with Vesta. For $\alpha = 15°, 30°$, these maxima are 2.74%, 1.63% for Vesta against 1.91%, 1.60% for Iris. This difference is easily explained by the fact that the Vesta polyhedron model is more refined than Iris in the area where the polarization is maximum, such that a single facet is allowed to reach a higher degree of polarization. The difference in maximum value between phase angles is explained by the area where the maximum is located. In Figure 3.3 (*top left, middle left*), this area is the edge on the left around the y-axis, whereas in Figure 3.3 (*top right, middle right*) these areas are the edge to the top and bottom around the z-axis. Apparently, the highly polarizing area to the left is shaded as soon as the phase angle passes a certain value between 15° and 30°. This shaded area effect was seen for Kleopatra as well, in Figure 2.7 (*right*). For Itokawa, the shaded area is more than half of the depicted area in Figure 3.3 (*top*), because the phase angles are well above 45°. Maximum facet-specific degree of polarization values are 5.63%, 9.41% for $\alpha = 50°, 70°$, such that the colorbar values are 0 to 10. Even for these high phase angles, the areas that polarize most are still the top and bottom areas as defined before. It is not unexpected that a higher phase angle results in a higher degree of polarization. Phase-polarization curves for ARM results and for polarimetric data are further discussed in Section 3.3.

3.3. Phase-polarization curves

Validating ARM output means disk-integrated degree of polarization values have to be calculated for phase angles that match the phase angles of available data. A renown source for polarimetric data is the APD (Lupishko, 2014), where data can be found in the format (*asteroid number, asteroid name, observation date, filter (radiation wavelength), phase angle, degree of polarization, direction of polarization, proper degree of polarization, observatory, publication*). The proper degree of polarization is described as *"degree of polarization in the proper coordinate system counted off from the perpendicular to the scattering plane:* $P(r) = P\cos 2Q(r)$, *where* $Q(r)$ *is the position angle in the proper coordinate system"*, such that polarization values have a minus sign if $Q(r)$ is around 90°, which is a common value. These proper degree of polarization values and their associated phase angles are used for validation purposes here.

In order to correctly cover the effect of the asteroid's orientation in ARM, at least a couple of different orientation simulations should be done of which the averaged disk- and time-integrated degree of polarization is taken. Figure 3.4 (*left*) shows the disk-integrated ARM output for the four asteroids used in Section 3.2 and the verification sphere from chapter 2. For all asteroids except Itokawa, for each phase angle, the 10 blue dots represent 10 orientations with $\phi_{\text{orientation}} = \{0°, 36°, 72°, \ldots 324°\}$, together covering one full azimuthal rotation. Itokawa only has 6 blue dots per phase angle, due to the great computational effort the Itokawa polyhedron requires, representing 6 orientations with $\phi_{\text{orientation}} = \{0°, 60°, 120°, \ldots 300°\}$. The black dots represent the disk- and orientation-integrated degrees of polarization, and are good candidates for comparison with the validation data. For each asteroid, a third order polynomial curve has been fitted to the black dots to give an impression of the general relation between polarization and phase angle for the martian analog scattering model. Figure 3.4 (*right*) shows the polarimetric data for asteroids (7) Iris, (4) Vesta and (25143) Itokawa (Lupishko, 2014), the latter of which is chosen to include polarization behavior for large phase angles. Following these data, the distinction is made between data points acquired using different filters, indicated by the colors of the dots. Additionally, for each asteroid, again a third order polynomial curve has been fitted to the data, ignoring the filter. See the caption of Figure 3.4 for the explanation of the marker shapes and colors. Additional references behind the polarimetric data for Iris are Zellner et al. (1974); Zellner and Gradie (1976); Broglia and Manara (1990); Gil-Hutton et al. (2011), for Vesta are Zellner et al. (1974); Zellner and Gradie (1976); Lupishko et al. (1989); Belskaya et al. (1987) and for Itokawa are Cellino et al. (2005).

A noticeable difference between the validation data and ARM output is that the validation data of Iris and Vesta have significant negative parts for $\alpha < 30°$. As was thoroughly discussed in Sibbing (2017), this negative surge is very common for asteroid phase-polarization curves. ARM output has no negative values at all, although the polynomial fits of Kleopatra, Itokawa and the sphere drop marginally below zero in a very narrow interval. Another difference is that Itokawa's validation data points reach as high as 5-7% for $\alpha \approx 70°$, while ARM output only reaches its maximum of about 3% at $\alpha \approx 105°$, both for Itokawa itself and for Kleopatra and the sphere. The lack of a negative surge for small phase angles and the slow increase for medium and

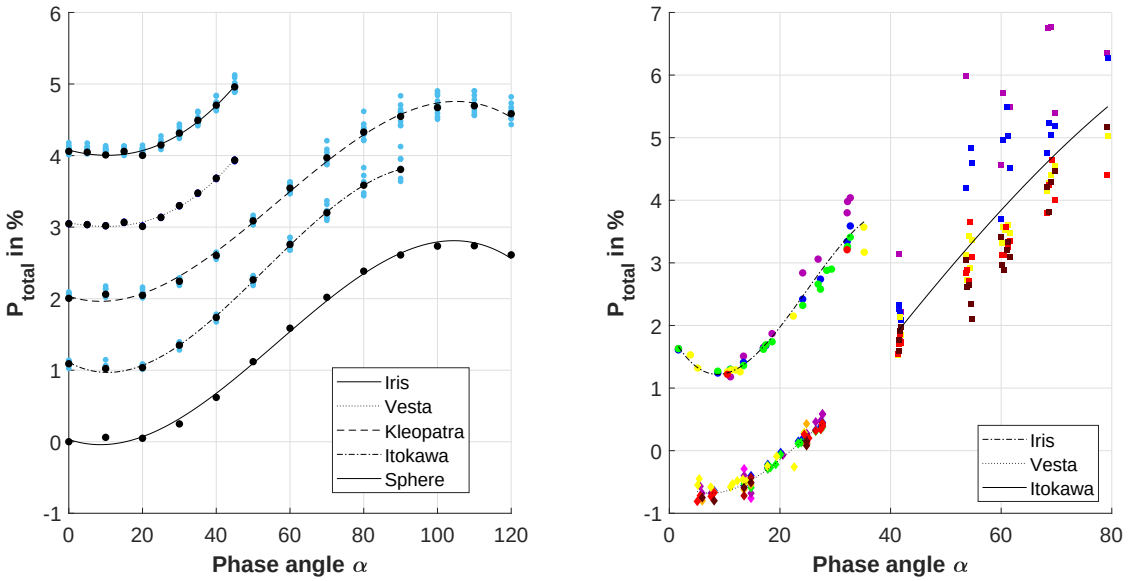

Figure 3.4: *Left*: Phase plot of the degree of polarization for asteroids (7) Iris, (4) Vesta, (216) Kleopatra and (25143) Itokawa and the verification sphere, as generated using the martian analog scattering model. Phase angles are 0° to 45° with steps of 5° for Iris and Vesta and 0° to 120° with steps of 10° for Kleopatra, Itokawa and the sphere. For convenience, the phase plots for Iris, Vesta, Kleopatra and Itokawa are vertically shifted by 4%, 3%, 2% and 1%, respectively. *Right*: Phase plot of the proper degree of polarization, as obtained from the APD, for asteroids (7) Iris (*circles*), (4) Vesta (*diamonds*) and (25143) Itokawa (*squares*). The colors of the dots correspond to: pink - UV (333 nm), purple - UV (362 nm), blue - Blue (435 nm), green - Green (518 nm), yellow - Visible (559 nm), orange - Orange (645 nm), red - Red (685 nm), maroon - Near-infrared (883 nm), brown - Infrared (952 nm). For convenience, the data of Iris is vertically shifted by 2%.

large phase angles are major defects of the phase-polarization curve for this martian analog scattering model, which leave room for improvement for the surface scattering model.

Putting the fit of ARM curve aside, there is another interesting aspect to the polarimetric data of Itokawa, which is the wavelength dependency. On average, the values for UV (362 nm) are highest, followed by Blue (435 nm), Visible (559 nm), Red (685 nm) and Infrared (952 nm). Even in the Iris data, the UV (362 nm) slightly rises above the other wavelengths for phase angles between approximately 25° and 35°, although this is less clear than with Itokawa. A global correlation between short wavelength and high degree of polarization can be concluded, a relation which can vary per asteroid, as will be shown for Phaethon in Section 3.4.

3.4. Fitting Phaethon polarimetric data

This section has been left out this version of the thesis, for reasons of publication by (Cellino et al., 2018).

Conclusions

Surface reflection measurements (flux and polarization) can detect many characteristics of an asteroid. Polarimetric observations, which are emphasized here, are useful to detect characteristics such as the surface composition and the shape and orientation of the asteroid. The flux is decided by properties such as the size and brightness of an asteroid and the distance from the observer to it. An advantage of the polarization is that it does not depend on the size and distance to an asteroid. Both parameters are simulated here. No complete model for the simulation of asteroid surface reflection and polarization existed as of yet (incorporating irregular shape, as opposed to a spherical shape), which is why ARM is introduced adequately.

ARM is a useful tool to simulate polarization and flux observations of an asteroid, comet or dwarf planet, in which the shape model is taken into account. For the implementation of ARM, the Planetary Reflection Model was used as a basis (Rossi et al., 2018). Unlike the base code, ARM can compute the flux and polarization signals of irregularly shaped bodies and use a triangle polyhedron shape model as input, including shape models of a hypothetical asteroid of which the shape and size are not certain as of yet. Furthermore, ARM can simulate any phase angle, any asteroid orientation, and a 2-dimensional pixel-based view of the reflected flux and polarization signals, resembling the output that an instrument's detector would give when observing the object. To do this, the working principle of ARM is based on elementary theoretical work on polarization such as Hansen and Travis (1974) and radiative transfer through the use of Fourier series expansions of reflection matrices (De Haan et al., 1987). These Fourier series expansions are generated by an external program (Rossi et al., 2018), called Fourier Series Program here.

The Fourier Series Program is of a level of importance that is not to be underestimated: the output of this program defines the asteroid's surface scattering model of each facet of the subject polyhedron, together defining the polarization characteristics of the asteroid to a large extent. As input for this program, scattering matrix elements of a certain sample material are used, which can either be found in databases such as the Amsterdam-Granada Light Scattering Database (Muñoz et al., 2012) or can be generated through setting user-defined material characteristics in a program such as SIRIS (Muinonen and Nousiainen, 2003). Both sources were used here, creating surface scattering models for a martian analog material, an olivine rock sample, three artificial materials with specifically chosen refractive indices and size parameters and four semi-artificial variants of the iron oxide called hematite. The resulting phase-polarization curves as generated with ARM, using these surface scattering models, were used to fit polarimetric data of (7) Iris, (4) Vesta and (25143) Itokawa and the recently acquired polarization data of (3200) Phaethon in greater detail. Finally, Asteroid (216) Kleopatra was used in the verifications because of its irregular shape.

Results of ARM come in two forms:

- The first form consists of spatially resolved 3-dimensional flux and polarization images of the asteroid under investigation in which the phase angle and the asteroid orientation are constant.
- The second form consists of disk-integrated phase-polarization or phase-flux curves in which a large range of phase angles is shown and in which various orientations are compared. This is a convenient form to compare asteroids and surface scattering models.

Results of the first form conveniently show the distribution of the flux or degree of polarization across the surface of the asteroid and offer insight in the effect of the phase angle or an asteroids orientation on these two. Also, these result can be compared to spatially resolved data, if available. Results of the latter form offer an overview of differences between surface scattering models, asteroid orientations and the effect of the irregularity of an asteroid's shape. Furthermore, they can be used to fit polarimetric data. Available polarimetric data often come in a variety of radiation wavelengths. Among surface scattering models of the hematite vari-

ants, this is incorporated adequately through the predefined material characteristics. As such, one is able to analyze the effect of wavelength in phase-polarization and phase-flux curves.

Spatially resolved and phase-polarization results for Iris, Vesta, Kleopatra and Itokawa were all generated using the martian analog surface scattering model, which did not offer a good fit to the available polarimetric data, as expected. The negative surge for small phase angles, which is common for many asteroids and also appears in the polarimetric data of Iris and Vesta, was not seen in ARM phase-polarization curves. This surge is caused by coherent backscattering and/or shadow hiding (Sibbing, 2017), effects which are not accounted for in the surface scattering models used here. Apart from the missing negative surge, the degree of polarization as generated by ARM is simply not high enough to fit to the data of any of the asteroids for medium phase angles. Despite the bad fit of these results to the polarimetric data, the spatially resolved data show some features worth mentioning. For small phase angles, the polarization pattern across different asteroid's surfaces is characterized by zero degree of polarization in the center, low around the center and high near the edge of the asteroid, in a near-circularly symmetric way. With increasing phase angle, this pattern only changes moderately: the degree of polarization in the center rises to the same level as the area around the center but the edge still presents the highest values, especially the edges in the direction perpendicular to the scattering plane. It is noted, however, that because these results are not so trustworthy, these features are not necessarily seen in real observations.

Asteroid Phaethon was studied into greater detail, because of the newly acquired, still unpublished results of Cellino et al. (2018). Phaethon is a small B-type asteroid with an extremely eccentric orbit (perihelion 0.14 AU, aphelion 2.40 AU) that crossed Earth's orbit very close to Earth in December 2017. Its rotational period is $P = 3.603958$ hours (Hanuš et al., 2016). A total of 96 data points observed in four wavelengths (infrared, red, visible, and blue), under phase angles ranging from 36° to 116°, offer interesting information about Phaethon's phase-polarization curves. Compared to other asteroid's phase-polarization curves, Phaethon's is astoundingly steep, reaching $P_{\text{l}} = 20\%$ at 70° phase angle and $P_{\text{l}} = 40\%$ at 110° phase angle. Phaethon's data is analyzed both in its full range and in smaller groups, here. The data were acquired over the course of seven evenings in December 2017, which makes seven groups of data collected over the period of a couple of hours each. The larger of these groups typically contain 15-25 data points, enough to distinguish the four wavelengths and fit a simple curve to data points of each wavelength within the group. The typical pattern regarding results for different wavelengths is that infrared radiation shows the highest degree of polarization, followed by red, visible and blue radiation, which all data points but five follow. Besides, in the curves for one wavelength over the course of one and several night, the variations due to the rotational motion of Phaethon, are seen.

Some seven different surface scattering models were evaluated in ARM to fit Phaethon's data. The artificial materials simulations resulted in three relatively good fits to the data, especially #1 for small and medium phase angles and #2 for high phase angles (see Table 3.1). The degree of polarization for these surface scattering models is overall only slightly lower than Phaethon's. The hematite variants simulations have worse fits: all four overall have significantly lower degrees of polarization. The hematite variants did, however, show the same degree of polarization order among wavelength curves: infrared highest, blue lowest. This makes the combination of both groups of surface scattering models probably the best: the refractive indices of the artificial materials and the wavelength dependency of the hematite variants. Experimenting with additional surface scattering models is discussed later. Like Phaethon's data, ARM data were subdivided into groups for each evening. On that scale, the differences between surface scattering models are similar to those for the entire phase angle range. A more interesting feature is the periodicity in the degree of polarization due to Phaethon's rotational motion and shape and size variations, which all results show alike. During two nights, results are simulated over a period long enough to cover a full rotation, which allows the detection of repetitive features in the phase-polarization curve. Also, across different nights, repetitive features appear again after an integer number of rotations. Detecting these features for Phaethon requires at least about 20 data points per rotation, or one data point each 10 minutes, given that Phaethon's shape is moderately irregular.

Other results that were obtained by allowing 10 different orientations per phase angle, over a range of phase angles that roughly coincides with the phase angle range of Phaethon data, are estimates of the mean, minimum and maximum degree of polarization for a certain phase angle. These extremes, indicating the extremes of the effect of the asteroid orientation, appear to scale with the degree of polarization. The last set of ARM results consist of the flux-polarization curves of the seven surface scattering models, which generally appear

to show less differences among them than the phase-polarization curves, even between the groups of artificial materials and hematite variants. On the scale of a single evening, however, the relative variation in one phase-flux curve is larger than in one phase-polarization curve, apart from the flux too showing similar periodic features during one evening and across several evenings. In practice, the relative errors in the flux are higher than in the polarization, which should mean that both the surface characteristics and the rotational motion of Phaethon are easier to detect with polarization measurements than with flux measurements.

Recommendations

Many of the functionalities that were planned to be implemented in ARM within the framework of this thesis, were indeed realized. Among them are: to use any (irregularly shaped) asteroid model, to use any surface scattering model, to use any asteroid orientation and phase angle, to determine and remove self-shading regions, to determine local surface reflection and polarization and to determine disk-integrated reflection and polarization.

Most decisive for the polarization pattern of ARM output is the surface scattering model, acquired from the Fourier Series Program. It was clear from ARM phase-polarization fits to polarimetric data, both for asteroids Iris, Vesta and Itokawa and for special case Phaethon, that the correct surface scattering models for all of them are yet to be found. This should be realized by implementing the correct physical properties of asteroid polarization, resulting in negative polarization for small phase angles, which are currently missing in the model. In order to correctly fit ARM data to the positive part of an asteroid's phase-polarization curve, these improvements are not needed. The fits to Phaethon were already very close, so one is invited to find a better fit using the surface scattering models that can be generated at the moment.

For Phaethon, the most interesting fits were the close-ups in which the asteroid can be seen rotating around its pole. It is recommended to try to improve these fits and produce additional, even more insightful plots. In future polarimetric surveys, the extremes of the degree of polarization across orientations as a function of the phase angle in these close-ups can be used to assess the correctness of the match of the surface scattering model with the asteroid. Also, an alternative program to the ARM could be implemented to process observational data and retrieve asteroid characteristics from them.

Apart from the aforementioned improvements, some aspects of ARM code could be improved as well. Below, a summary of the discussed improvements and these ARM improvements, is given.

- Implement coherent backscattering and shadow hiding (together the physical causes of the opposition effect), such that negative polarization can be simulated. Until a model with these improvements is available, no asteroid's negative surge in its phase-polarization curve can be modeled.
- Experiment with other surface scattering models than the currently used ones to find an even better fit for medium and high phase angles. It is expected that changing the refractive index of the current best fitting model only modestly should already lead to a better fit.
- Experiment with more than one surface scattering model combined on the surface of the asteroid model, which should be very interesting and especially more realistic.
- Improve the close-up fits further by assuming the correct orientation instead of only the correct periodicity of the rotation.
- Produce a series of curves with slightly different starting orientations but still the correct rotational period, so to see the effect of these small orientation differences on the phase-polarization curve.
- Produce various extreme curves and fit them alongside each other for different wavelengths, to provide an even more complete image of the expected phase-polarization curves.
- Extend ARM by adding an alternative program that estimates the shape and rotational period based on polarimetric data. This so-called inversion technique already exists for flux measurements but not for polarization measurements.
- Improve user-friendliness through improving the input method of the asteroid's and observer's locations for a single simulation and the input method of the asteroid orientation change over several simulations.

- If data such as Phaethon's is analyzed more often, improve ARM by adding complete coupling between the asteroid's orbit and orientation with respect to the observer and the observer's orbit, whether the observer's location is Earth or a spacecraft.
- Regarding the computational efficiency of ARM, the part that should be improved first is the self-shading algorithm. It has been stated that the number of iterations in this algorithm is currently the number of facets that is left after excluding facets with $\mu_0 < 0$, squared, plus the number of facets that is left after excluding facets with $\mu < 0$, squared. The reason it is currently implemented in this way is that it is a convenient and robust method, but not so efficient after all. As a result, large asteroid polyhedron models are computationally very costly to process.

Regarding the Phaethon data, some recommendations are done, although this is hindsight. By having more observations of the same wavelength in a short period of time, more information about the asteroid's shape and rotational period could be retrieved from the data. This should be a consideration if an observations survey is planned in the future for a certain asteroid of which the rotational period and the shape is unknown: either observations in different wavelengths to gain information about the asteroid's surface materials or more observations for one wavelength to improve the shape estimate. Going for the latter option, the aforementioned inversion technique could be used to solve for the shape.

Certainly, if a new asteroid is discovered and no knowledge whatsoever is available regarding it, except for its orbit, one could choose to start with polarimetric observations instead of flux observations, the latter of which is the more common path. As shown with ARM, both have a good record in resolving the shape of an asteroid, if the relative error in both data is equal. However, if the presumed error in the flux is relatively large, for example because the asteroid is very faint, polarimetric observations are a promising alternative. In those measurements, one is able to cancel errors which are constant for all flux intensities used to calculate the degree of polarization, because the polarization is a relative measure. Example errors that cancel as a result are environmental/atmospheric errors and relative instrument errors. Unfortunately, one cannot detect the size of an object using only the polarization, which is why the flux is needed eventually. The combination of the two is ideal: polarization measurements can be used for the shape and surface composition of the asteroid, and to fit the flux observations in order to retrieve the size of the asteroid.

Bibliography

AIP. Johnson-Cousins UBVRI filter curves. `http://www.aip.de/en/research/facilities/stella/instruments/data/johnson-ubvri-filter-curves`, 2018.

S. Bagnulo, I.N. Belskaya, K. Muinonen, G.P. Tozzi, M.A. Barucci, L. Kolokolova, and S. Fornasier. Discovery of two distinct polarimetric behaviours of trans-Neptunian objects. *Astronomy & Astrophysics*, 491(2):L33–L36, 2008.

D.R. Bates. Rayleigh scattering by air. *Planetary and Space Science*, 32(6):785–790, 1984.

I. Belskaya, A. Stinson, S. Bagnulo, A. Christou, and K. Muinonen. Polarimetric observations of Jupiter Trojans. In *European Planetary Science Congress 2014, EPSC Abstracts, Vol. 9, id. EPSC2014-727*, 2014.

I.N. Belskaya, D.F. Lupishko, and N.M. Shakhovskoi. Negative polarization spectra for five asteroids. *Soviet Astronomy Letters*, 13:219, 1987.

I.N. Belskaya, A. Cellino, R. Gil-Hutton, K. Muinonen, Y. Shkuratov, et al. Asteroid polarimetry. *Asteroids IV*, 1: 151–163, 2015.

W.F. Bottke. *Asteroids III*. University of Arizona Press, 2002.

P. Bourke. Sphere Generation. `http://paulbourke.net/geometry/circlesphere/`, 1992.

P. Broglia and A. Manara. A search for rotational variations in the optical polarization of 3 Juno and 7 Iris. *Astronomy and Astrophysics*, 237:256–258, 1990.

A. Cellino, F. Yoshida, E. Anderlucci, P. Bendjoya, M. Di Martino, M. Ishiguro, A.M. Nakamura, and J. Saito. A polarimetric study of Asteroid 25143 Itokawa. *Icarus*, 179(2):297–303, 2005.

A. Cellino, M. Delbò, P. Bendjoya, and E.F. Tedesco. Polarimetric evidence of close similarity between members of the Karin and Koronis dynamical families. *Icarus*, 209(2):556–563, 2010.

A. Cellino, S. Bagnulo, P. Tanga, B. Novaković, and M. Delbo. A successful search for hidden Barbarians in the Watsonia asteroid family. *Monthly Notices of the Royal Astronomical Society: Letters*, 439(1):L75–L79, 2014.

A. Cellino, E. Ammannito, G. Magni, R. Gil-Hutton, E.F. Tedesco, I.N. Belskaya, M.C. De Sanctis, S. Schröder, F. Preusker, and A. Manara. The Dawn exploration of (4) Vesta as the 'ground truth' to interpret asteroid polarimetry. *Monthly Notices of the Royal Astronomical Society*, 456(1):248–262, 2016.

A. Cellino, S. Bagnulo, G. Borisov, P. Bendjoya, and J.-P. Rivet. Unpublished polarimetry observations of Phaethon. Unpublished data, 2018.

J.F. De Haan, P.B. Bosma, and J.W. Hovenier. The adding method for multiple scattering calculations of polarized light. *Astronomy and Astrophysics*, 183:371–391, 1987.

M. Delbo, A. Cellino, and E.F. Tedesco. Albedo and size determination of potentially hazardous asteroids:(99942) Apophis. *Icarus*, 188(1):266–269, 2007.

M. Devogèle, A. Cellino, S. Bagnulo, J.-P. Rivet, P. Bendjoya, L. Abe, C. Pernechele, G. Massone, D. Vernet, P. Tanga, et al. The Calern Asteroid Polarimetric Survey using the Torino polarimeter: assessment of instrument performances and first scientific results. *Monthly Notices of the Royal Astronomical Society*, 465(4): 4335–4347, 2016.

A. Dollfus, M. Wolff, J.E. Geake, L.M. Dougherty, and D.F. Lupishko. Photopolarimetry of asteroids. *Asteroids II*, pages 594–616, 1989.

Audouin Dollfus. Étude des planètes par la polarisation de leur lumière. *Supplements aux Annales d'Astrophysique*, 4:3–114, 1957.

J. Escobar-Cerezo. *Dust in planetary and cometary atmospheres: an experimental and computational study based on the analysis of a lunar dust analog*. PhD thesis, Instituto de Astrofísica de Andalucía, 2018.

R. Gaskell, J. Saito, M. Ishiguro, T. Kubota, T. Hashimoto, N. Hirata, S. Abe, O. Barnouin-Jha, and D. Scheeres. Gaskell Itokawa Shape Model V1.0. HAY-A-AMICA-5-ITOKAWASHAPE-V1.0. `https://sbn.psi.edu/pds/resource/rshape.html`, 2008.

T. Gehrels. Photometric Studies of Asteroids. V. The Light-Curve and Phase Function of 20 Massalia. *The Astrophysical Journal*, 123:331, 1956.

R. Gil-Hutton et al. Polarimetric survey of main-belt asteroids-I. Results for fifty seven S-, L-, and K-type objects. *Astronomy & Astrophysics*, 529:A86, 2011.

J.E. Hansen and L.D. Travis. Light scattering in planetary atmospheres. *Space Science Reviews*, 16(4):527–610, 1974.

J. Hanuš, M. Delbo, D. Vokrouhlickỳ, P. Pravec, J.P. Emery, V. Alí-Lagoa, B. Bolin, M. Devogèle, R. Dyvig, A. Galád, et al. Near-Earth asteroid (3200) Phaethon: Characterization of its orbit, spin state, and thermophysical parameters. *Astronomy & Astrophysics*, 592:A34, 2016.

A.W. Harris, J.W. Young, L. Contreiras, T. Dockweiler, L. Belkora, H. Salo, W.D. Harris, E. Bowell, M. Poutanen, R.P. Binzel, et al. Phase relations of high albedo asteroids: The unusual opposition brightening of 44 Nysa and 64 Angelina. *Icarus*, 81(2):365–374, 1989.

J.W. Hovenier and C.V.M. Van der Mee. Fundamental relationships relevant to the transfer of polarized light in a scattering atmosphere. *Astronomy and Astrophysics*, 128:1–16, 1983.

JPL. HORIZONS Web-Interface. `https://ssd.jpl.nasa.gov/horizons.cgi`, 2018.

EC Laan, H Volten, DM Stam, O Munoz, JW Hovenier, and TL Roush. Scattering matrices and expansion coefficients of martian analogue palagonite particles. *Icarus*, 199(1):219–230, 2009.

D. Lupishko. Asteroid Polarimetric Database V8.0. EAR-A-3-RDR-APD-POLARIMETRY-V8.0. `https://sbn.psi.edu/pds/resource/apd.html`, 2014.

D.F. Lupishko, I.N. Belskaya, O.I. Kvaratskheliya, N.N. Kiselev, A.V. Morozhenko, and N.M. Shakhovskiy. Polarimetry of Vesta in 1986 opposition. *JPRS Report Science Technology USSR Space*, 2, 1989.

MATLAB. Interpolation Methods. `https://nl.mathworks.com/help/curvefit/interpolation-methods.html`, 2018a.

MATLAB. Smoothing Splines. `https://nl.mathworks.com/help/curvefit/smoothing-splines.html`, 2018b.

P. Michel, F.E. DeMeo, and W.F. Bottke. *Asteroids IV*. University of Arizona Press, 2015.

K. Muinonen. Electromagnetic scattering by two interacting dipoles. In *Proceedings of URSI Electromagnetic Theory Symposium*, pages 428–430, 1989.

K. Muinonen and T. Nousiainen. SIRIS - Free Software for Light Scattering by Small Particles. `https://wiki.helsinki.fi/display/PSR/SIRIS`, 2003.

K. Muinonen, J. Piironen, Y.G. Shkuratov, A. Ovcharenko, and B.E. Clark. Asteroid photometric and polarimetric phase effects. *Asteroids III*, pages 123–138, 2002.

O. Muñoz. The Granada Light Scattering Database. `https://www.iaa.csic.es/scattering/granada/measurements/cosmic/index.html`, 2018.

O. Muñoz, F. Moreno, D. Guirado, D.D. Dabrowska, H. Volten, and J.W. Hovenier. The Amsterdam-Granada light scattering database. *Journal of Quantitative Spectroscopy and Radiative Transfer*, 113(7):565–574, 2012.

NASA. Small Body Optical Shape Models V2.1. EAR-A-5-DDR-SHAPE-MODELS-V2.1. https://sbn.psi.edu/pds/resource/oshape.html, 2018.

C. Neese. Small Body Radar Shape Models V2.0. EAR-A-5-DDR-RADARSHAPE-MODELS-V2.0. https://sbn.psi.edu/pds/resource/rshape.html, 2004.

S.J. Ostro, R. Scott, M.C. Nolan, J.-L. Margot, D.J. Scheeres, D.B. Campbell, C. Magri, J.D. Giorgini, D.K. Yeomans, et al. Radar observations of asteroid 216 Kleopatra. *Science*, 288(5467):836–839, 2000.

S.J. Ostro, R.S. Hudson, M.C. Nolan, J.-L. Margot, D.J. Scheeres, D.B. Campbell, C. Magri, J.D. Giorgini, and D.K. Yeomans. ASTEROID RADAR SHAPE MODELS, 216 KLEOPATRA. EAR-A-5-DDR-RADARSHAPE-MODELS-V2.0:RSHAPES-216KLEOPATRA-200405. https://sbn.psi.edu/pds/resource/rshape.html, 2004.

W.H. Press, S.A. Teukolsky, W.T. Vetterling, and B.P. Flannery. *Numerical recipes in Fortran 90*, volume 2. Cambridge university press Cambridge, 2 edition, 1996.

L. Rossi, J. Berzosa-Molina, and D.M. Stam. PyMieDAP: a Python-Fortran tool to compute fluxes and polarization signals of (exo)planets. *Astronomy & Astrophysics*, 2018.

H.M. Schmid, F. Joos, E. Buenzli, and D. Gisler. Long slit spectropolarimetry of Jupiter and Saturn. *Icarus*, 212 (2):701–713, 2011.

Y.G. Shkuratov, K. Muinonen, E. Bowell, K. Lumme, J.I. Peltoniemi, M.A. Kreslavsky, D.G. Stankevich, V.P. Tishkovetz, N.V. Opanasenko, and L.Ya. Melkumova. A critical review of theoretical models of negatively polarized light scattered by atmosphereless solar system bodies. *Earth, Moon, and Planets*, 65(3):201–246, 1994.

Z.R. Sibbing. Asteroid Polarimetry with Spectropolarimeter for Planetary EXploration (SPEX). Literature review, Delft University of Technology, August 2017.

F. Snik, J.H.H. Rietjens, G. van Harten, D.M. Stam, C.U. Keller, J.M. Smit, E.C. Laan, A.L. Verlaan, R. ter Horst, R. Navarro, et al. SPEX: The Spectropolarimeter for Planetary EXploration. page 77311B, 2010.

D.M. Stam, W.A. De Rooij, G. Cornet, and J.W. Hovenier. Integrating polarized light over a planetary disk applied to starlight reflected by extrasolar planets. *Astronomy & Astrophysics*, 452(2):669–683, 2006.

P.C. Thomas, R.P. Binzel, M.J. Gaffey, B.H. Zellner, A.D. Storrs, and E. Wells. Vesta: Spin pole, size, and shape from HST images. *Icarus*, 128(1):88–94, 1997.

N. Umov. Chromatische Depolarisation durch Lichtzerstreuung. *Physikalische Zeitschrift*, 6:674–676, 1905.

G. van Harten. *Spectropolarimetry for planetary exploration*. Leiden Observatory, Faculty of Science, Leiden University, 2014.

J. Ďurech. Database of Asteroid Models from Inversion Techniques. http://astro.troja.mff.cuni.cz/projects/asteroids3D/web.php, 2018.

J. Ďurech, V. Sidorin, and M. Kaasalainen. DAMIT: a database of asteroid models. *Astronomy & Astrophysics*, 513(A46), 2010.

H. Volten, O. Muñoz, J.W. Hovenier, and R. Waters. The Amsterdam Light Scattering Database. https://www.iaa.csic.es/scattering/amsterdam/index.html, 2012.

R. Voors, S.G. Moon, S. Hannemann, J.H.H. Rietjens, G. van Harten, F. Snik, M. Smit, D.M. Stam, C.U. Keller, E.C. Laan, et al. Spectropolarimeter for planetary exploration (SPEX): performance measurements with a prototype. page 81760D, 2011.

Karel F Wakker. *Fundamentals of astrodynamics*. TU Delft Library, 2015.

E.W. Weisstein. Barycentric Coordinates. http://mathworld.wolfram.com/BarycentricCoordinates.html, 2018a.

E.W. Weisstein. Heron's Formula. http://mathworld.wolfram.com/HeronsFormula.html, 2018b.

E.W. Weisstein. Rotation Matrix. http://mathworld.wolfram.com/RotationMatrix.html, 2018c.

B. Zellner and J. Gradie. Minor planets and related objects. XX-Polarimetric evidence for the albedos and compositions of 94 asteroids. *The Astronomical Journal*, 81:262–280, 1976.

B. Zellner, T. Gehrels, and J. Gradie. Minor planets and related objects. XVI-Polarimetric diameters. *The Astronomical Journal*, 79:1100–1110, 1974.